Ship Wakes Generated in a Diffuse Internal Layer

Prepared by: J.K.E. Tunaley
London Research and Development Corporation
114 Margaret Anne Drive,
Ottawa, ON K0A1L0

Contractor's Document Number: 2014-12-001
PWGSC Contract Number: W7719-4501203540
Scientific Authority: Paris W. Vachon

The scientific or technical validity of this Contract Report is entirely the responsibility of the Contrator and the contents do not necessarily have the approval or endorsement of the Department of National Defence of Canada.

Contract Report
DRDC-RDDC-2015-C093
January 2015

© Her Majesty the Queen in Right of Canada, as represented by the Minister of National Defence, 2015

© Sa Majesté la Reine (en droit du Canada), telle que représentée par le ministre de la Défense nationale, 2015

Abstract

This report describes the background, theory and simulation of the internal wave wake from ships. Realistic models of both internal layers and hulls are employed. The internal layer models are based on published vertical profiles of the Brunt-Väisälä frequency. Two basic profiles are employed. The first is a profile appropriate to the Strait of Gibraltar and is modeled using a Lorentzian distribution; the parameters are the peak Brunt-Väisälä frequency, its depth and the width of the distribution. If required, these can be altered to apply to other situations. The second profile is appropriate to that existing during the Loch Linnhe trials in Scotland.

The hull models represent warship and merchant ship hulls. The warship hull model is a modified Taylor model and the block coefficient can be adjusted continuously within suitable limits; the parent model was based on a twin screwed cruiser. The merchant ship model was developed by the David Taylor Model Basin and applies to single screwed ships. There are 5 separate models covering a range of block coefficients. The Wigley model, which resembles a canoe, a single source model and a simple source and sink model (doublet) are available in part for diagnostics.

The simulations successfully reproduce some observations of wakes during the Loch Linnhe trials, in which wakes with significant structure were generated. Wakes generated on the Gibraltar layer appear to be on the edge of detectability by airborne or space-borne high resolution radar and consist mainly of a V-shape with little structure in between the arms.

Executive Summary

A full understanding of internal wave wakes is required if these wakes are to be useful for maritime surveillance. The objective of this work is to gain this understanding by numerically simulating wakes for realistic internal layers using realistic hull models moving at operational speeds. Simplified layer models can be useful and previous work has shown that rough agreement with observations can be achieved under some circumstances. Realistic models offer the opportunity for more reliable conclusions about wake visibility, for example in radar imagery. However, the present study is limited to the super-critical case when the ship speed is greater than the maximum wave velocity.

Previous layer models have included the discrete type where a fluid of low density, such as fresh water, lies on a fluid of high density, such as salt water, forming a discrete horizontal interface on which waves can propagate. At the next level, the layer can comprise a thick layer of constant Brunt-Väisälä (B-V) frequency sandwiched between fluids of constant but differing densities. In practice the B-V frequency changes continuously and may exhibit several peaks. The presence of irregularities in the B-V frequency and its slow fall-off at depth introduce some technical problems in the numerical calculations. Solutions to these problems are addressed.

The simulations have been validated by comparing the results with observations from the Loch Linnhe trials. Agreement with the simulated and observed crest patterns is excellent when the published Loch Linnhe vertical profile is used. For the ships in the trials, the predicted amplitudes are also of the correct magnitude; unlike for the discrete layer model, no adjustments are needed.

Naturally occurring internal waves in the ocean are very common in littoral areas and can be observed using satellite borne optical sensors and high resolution radar. Their existence implies the presence of significant internal layers. The layer characteristics are described in the published literature. In the open ocean, natural internal waves are less common and there is a dearth of information. However, layers should exist, especially during summer in the tropics.

The wake and its detectability depend on a number of factors. The principal factors associated with the ship appear to be its principal dimensions (length, beam and draft), its block coefficient and its speed. The principal factors associated with the layer are its maximum B-V frequency, the depth and width of the layer and the presence and width of a mixed layer at the surface. The latter tends to suppress a wake and the presence of mixed layers probably explains why internal wave wakes are not frequently observed in radar imagery.

For layers appropriate to littoral ocean conditions, the results suggest that internal wave wakes generated by shipping should commonly occur but are usually on or below the threshold of detectability using present radar technology. There is some expectation that

conditions can be identified when wakes can be detected reliably and that improvements to radar and other systems might be made to achieve a useful probability of detection.

Table of Contents

Ship Wakes Generated in a Diffuse Internal Layer i
Abstract i
Executive Summary ii
Table of Contents iv
Introduction 1
Internal Waves 4
Layer Models 6
Hull Models 7
Theory 12
Numerical Analysis 19
The Program 20
Simulation Results 21
Discussion 28
Wake Detectability 29
Conclusions 30
References 31
Appendix 1: Sturm-Liouville Theory 33
Appendix 2: The Crest Pattern and Wake Waves 35
Appendix 3: Integral Evaluation 37
Appendix 4: Matrix Approach 39
Appendix 5: Comparison of Discrete and Diffuse Layer Theories 41

Introduction

As noted in previous reports [1] [2], ship wakes and particularly those in space-borne high resolution radar images can be important for maritime surveillance. They can yield information about the ship course and speed and help to verify the data from other sensors, such as Automatic Identification Systems (AIS), which must be carried by large ships according to international maritime law. The purpose of this report is to examine the surface manifestation of internal wave wakes generated by ships using realistic models of both internal layers and ship hulls through numerical simulation. This is in contrast to previous reports and papers for which the model of the undisturbed layer was either a discrete horizontal planar interface bounding fluids of different density [3] or involved a few sections in which the density varied linearly with depth (e.g. [4]). In some cases the focus has been on the crest pattern (e.g. [6]).

This study is limited to the super-critical case when the ship speed is greater than the maximum speed of internal waves, which is typically less than 1 m/s and often much less. In the super-critical regime, which corresponds to operational speeds, the wake comprises only divergent waves with no transverse wave structure. As the ship speed increases, the wake becomes narrower. At speeds lower than the maximum wave speed, the wake comprises both divergent and transverse waves and its crest pattern resembles that of the Kelvin wake but the wake angle is greater than 19.5º. The presence of transverse waves can create a large drag on the ship and this is known as the "dead water" effect. Thus it is possible that the low speed case could also be important for wake detection.

The Loch Linnhe trials were conducted between 1989 and 1994 and provided documented internal wave wakes including radar images. Fortunately comprehensive documentation for one or two wakes is available in the open literature and, as in [2], this forms the observational data for comparison with simulations. Simulation of the high resolution radar image of a ship wake located on the surface of the sea requires an understanding of hydrodynamics, radar scattering and, for space-borne applications, Synthetic Aperture Radar (SAR) processing. To simplify the process, only the hydrodynamics is considered here. Radar imagery of gravity wave wakes (this class includes internal wave wakes) is affected by horizontal surface fluid flows associated with wakes and these are compared with those derived from measurements taken during the trials.

During the trials the sub-surface fluid flows were monitored as a function of time at various depths on a vertical line at a location near the ship's track [5]. In [2], using the discrete layer model it was shown that the crest pattern roughly matched the observed pattern and that surface flows of approximately the correct magnitude were predicted. However, it was not possible to match both the flow velocities and the number of oscillations in the time record simultaneously. The number of oscillations could be matched by increasing the assumed depth of the discrete interface but then the amplitudes were significantly reduced. As will be seen, this problem is overcome when the appropriate diffuse layer is modeled.

The theory and implementation of the simulation of internal wave ship wakes has been sketched in the literature [4] and indeed a correspondence between simulations and internal wave wakes has been claimed, though a simplified layer model was employed. Realistic internal layer models are based on the Brunt-Väisälä (B-V) frequency vertical profile. The B-V frequency is the natural frequency of oscillation of a parcel of fluid that is displaced by a small vertical distance. In [4] the B-V frequency was constant over the layer and zero outside it so that a rectangular vertical profile was used. One purpose of this report is to describe the simulation process in detail (using a realistic profile) and to examine the effects of varying the parameters of the layer, the ship hull shape and the ship speed on the appearance of the wake and on the magnitude of the surface flows.

Large amplitude internal waves can develop into internal shocks and solitons; the waves can propagate over long distances while their shape hardly changes. Larger waves may break. These are non-linear effects. For small amplitude waves a linear theory may suffice and this should usually be appropriate for ship generated waves especially in the far wake. The correspondence between observed internal wake crest patterns and the theoretical predictions suggests that a linear theory is adequate. If ships were to generate soliton wakes, their wakes would be primarily in the form of a 'V' with little internal structure.

Wake formation can be understood in terms of gravity waves emanating from disturbances created by the movement of the hull through the water as it first pushes it aside and as it subsequently flows back into its previous position. If turbulence is neglected, the disturbances are stationary in the reference frame of the ship and this considerably simplifies the theory. Another simplification is possible if we focus on the far wake because the waves are dominated by dispersive effects and a wave packet that travels a large distance becomes closely sinusoidal, regardless of its initial shape; the distance traveled is determined by the group velocity. Because the disturbance is stationary in the reference frame of the ship, the wake, which travels along with it, is also stationary in this frame. This implies that each wave in the wake must satisfy a phase relation based on the phase velocity; the component of the ship velocity along the wave vector must be equal to the phase velocity. Otherwise a crest would not be stationary in this reference frame.

While the latter simplification involving the group velocity might seem restrictive, the approach is related to geometrical optics and closely resembles the mathematical methods of integration known as stationary phase and steepest descents. It is known that these methods frequently provide results that are approximately correct over a domain that is much broader than might reasonably be expected. Thus the "geometrical" method provides plausible results even close to the ship.

The theory and simulation of internal waves on a horizontal diffuse layer can be understood in terms of a waveguide analogy from electromagnetic theory. In a waveguide the waves within it are bounded by the walls and propagate between them, where they are reflected. Nevertheless, the propagation can be described by wave vectors parallel to the waveguide axis. At a given frequency there may be several possible wave vectors and

each one corresponds to a “mode”. Similarly, at a given frequency, which must be less than local B-V frequency, waves can propagate with a component in the vertical direction but are reflected before they reach a level at which the B-V frequency equals the wave frequency. Therefore the waves tend to be constrained to propagate within the layer. Outside these bounds, the wave amplitudes fall off exponentially in a manner that depends on the wave frequency, the B-V frequencies and how the latter vary with depth.

Wake simulation for the discrete internal layer has been described in previous reports [2] [3]. There are significant differences between the wakes produced on a discrete layer compared with those on a diffuse layer. The discrete layer is equivalent to a very narrow diffuse layer. While the B-V frequency of a diffuse layer is usually limited to about 0.1 rad/s (as in the Loch Linnhe trials) and is usually much less, that the B-V frequency in the discrete layer is technically infinite. These differences influence the crest pattern because, as just noted, the maximum frequency of horizontal waves on a layer is equal to the maximum B-V frequency of the layer. The lowest frequency waves in a wake tend to lie near the wake edge and the highest frequency waves near the wake axis. Therefore the finite upper limit to the B-V frequency affects those wake waves near the wake axis. The effect on the crest pattern is to shift the apex of subsequent crests backwards, so that there is a gap between each crest on the axis of the wake. This axis of course corresponds to the ship track. The lower the maximum B-V frequency, the greater the backward shift. In the case of a discrete layer there is no shift and all crests intersect at the wake apex.

Additional differences occur because waves can propagate with a vertical component. This implies that a disturbance actually located in the layer will produce waves directly and these can be of large amplitude and can propagate vertically through the layer; this tends to increase wake visibility. In comparison the disturbance on a discrete layer will usually be located some vertical distance away from it and its effect at the layer will be attenuated. Unfortunately broad layers tend to exhibit low B-V frequencies and the crest pattern shifts may reduce wake visibility. Thus, as far as detectability is concerned, these effects tend to act in opposition.

An example of a (airborne) radar image of a wake from the Loch Linnhe trials is shown in Figure 1. The radar frequency is at L-band and the ship, which was the Sir Tristram and appears as the bright object to the right, is traveling at a speed of 2 m/s. The length of the image corresponds to a distance of about 4 km and the original pixel size was about 4 m.

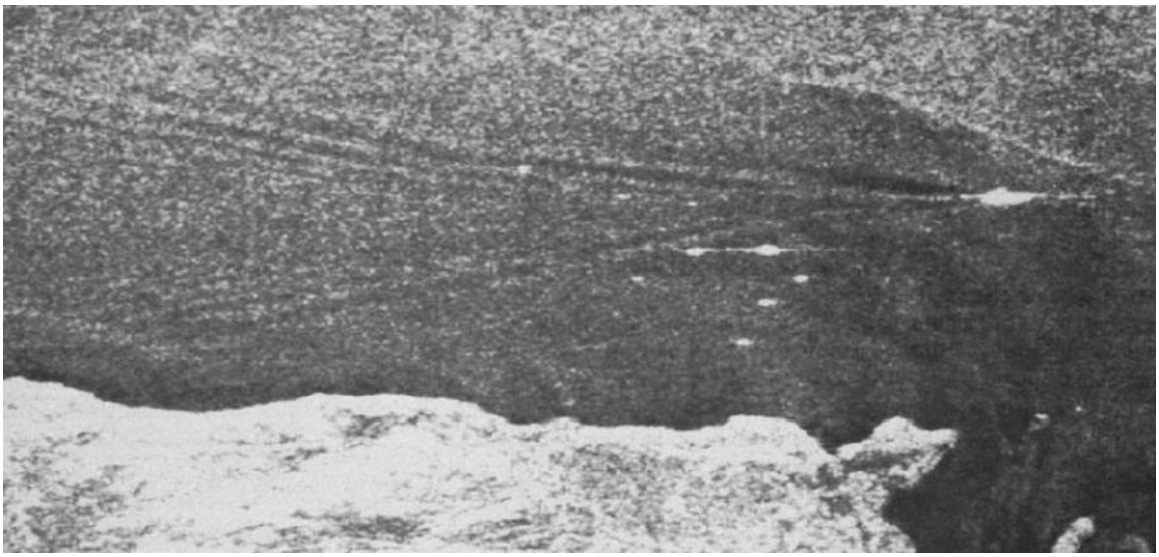

Figure 1. Sir Tristram wake. Ship speed is 2.0 m/s. From [5].

Internal Waves

When stratification of fluid density is present, internal waves can occur. These are gravity waves and their mechanism resembles that of the waves on the ocean surface. It is usually assumed that the stratification is horizontal so that the properties of the layer are described by vertical profiles, such as density and temperature. In fact the most useful profile is that of the B-V frequency. As noted, the B-V frequency is the frequency of vertical buoyancy oscillations of a small fluid parcel that has been disturbed from its equilibrium position and, in contrast to surface gravity waves, internal waves are three-dimensional.

Oceanic internal waves are frequently observed by space-borne Synthetic Aperture Radar (SAR). A useful description has been provided by Jackson et al. (2013) [7] as well as in [8]. The waves are usually a result of tidal flows over sills or other obstacles on the ocean floor. They are analogous to the waves on the surface of a stream that flows over a stone. However, naturally occurring internal waves that are observed by SAR are typically non-linear wave packets and individual waves develop into a soliton. Internal wave solitons are analogous to tidal bores that can occur on some rivers. In a sequence of tidal cycles, a train of internal solitons can be produced. The phase speed of the waves can vary between 0.3 m/s to over 3 m/s; amplitudes on the layer can range from a few metres to more than 100 m.

The waves are visible in SAR imagery because surface flows are induced that affect the radar scattering cross-section of the ocean [9]. These flows compress or expand the Bragg waves responsible for the radar backscattering. In addition, periodic horizontal flows can create bands of slicks, which tend to suppress the Bragg waves [7]. The waves can be distinguished from other features in radar imagery by the fact that natural internal waves appear in bands and the first or leading bright or dark crest is separated from the second by a slightly larger distance than that between the second and third. This is because large

amplitude waves move faster than small amplitude waves and the fact that the soliton amplitude tends to increase as the wave packet evolves and leading waves coalesce.

Internal waves in SAR imagery tend to be located on continental shelves, in straits and in marginal seas [7]. This is because not only does suitable horizontal stratification but also the conditions for wave generation exist. It does not imply that layers capable of supporting internal waves are not present in the open ocean. However, density variations associated with fresh water flowing over salt water will tend to be confined to coastal regions and the arctic (ice melt). In the open ocean, temperature variations are expected to be the main factor. Nevertheless, the global distribution of natural internal waves may be useful for estimating the likelihood of a significant layer in a given area of ocean.

Global Ocean Associates has created an atlas of internal wave occurrences [10]. This contains a chapter by Apel summarizing the background and theory of the waves. He remarks (in 2004) that the distribution of deep water internal waves is still a research project and this seems to be confirmed in [7]. The atlas contains details about the generation and interpretation of internal waves and the section on the Strait of Gibraltar is particularly interesting. The flow of the upper layer of ocean water is eastwards from the Atlantic Ocean through the Strait. The lower layer of denser water flows westward from the Mediterranean. Internal waves are generated by these flows over very pronounced bottom features, such as the Camarinal Sill. Waves are present year-round particularly on the eastern side of the Strait. In summer, waves can be produced by westward flows on the western side due to the presence of a strong thermocline in the Atlantic. The waves are strongest during the spring tide and weakest at neap tide. This effect is associated with the strength of the flows through the Strait.

An example of a B-V profile for the Strait of Gibraltar is provided in [10] and this is adopted for one canonical model in this report. Figure 2, from [8], shows the distribution of internal wave observations over a period from 2002 to 2004.

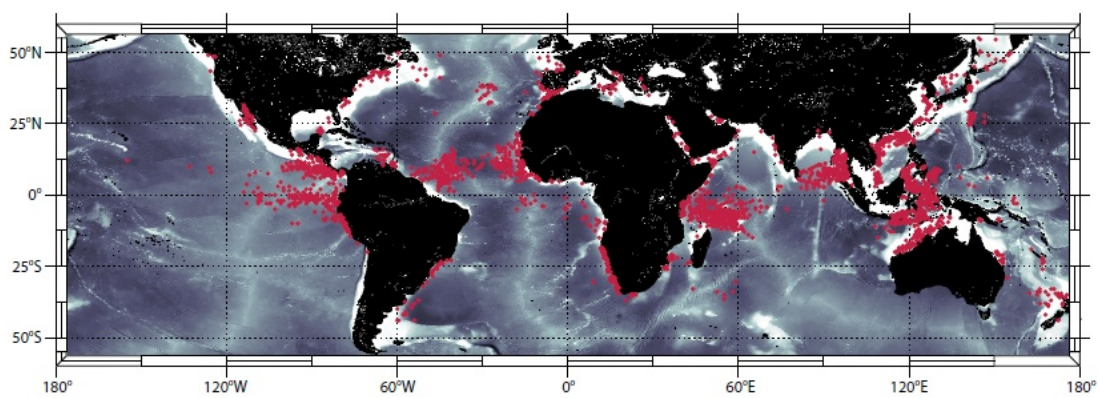

Figure 2. Locations of 3500 occurrences of non-linear internal waves
In MODIS true-color images from 2002 to 2004 (from [8]).

In summary, significant internal layers can certainly be found on most if not all continental shelves, especially in summer. They can also be found in the open ocean especially in the tropics during the summer.

Layer Models

Two basic models are employed for the vertical B-V frequency profile. The first relies on a Lorentzian distribution with depth. The parameters are the maximum B-V frequency, the depth of this peak and its width and the depth of the ocean. An example is shown in Fig. 3, which represents the profile off Gibraltar. The peak B-V frequency is 0.015 rad/s at a depth of 60 m. The width is 100 m. There is no mixed layer at the surface.

The second type of profile is read from a file and is believed to be representative of the profile during the Loch Linnhe trials. This is derived from Watson et al. [5] and is shown in Fig. 4. The layer is close to the surface and is quite narrow; the maximum B-V frequency is correspondingly greater than that of the Gibraltar profile. Again there is no significant mixed layer near the surface. As will be shown, a thick mixed layer tends to reduce the surface velocities and the likelihood of observing the wake.

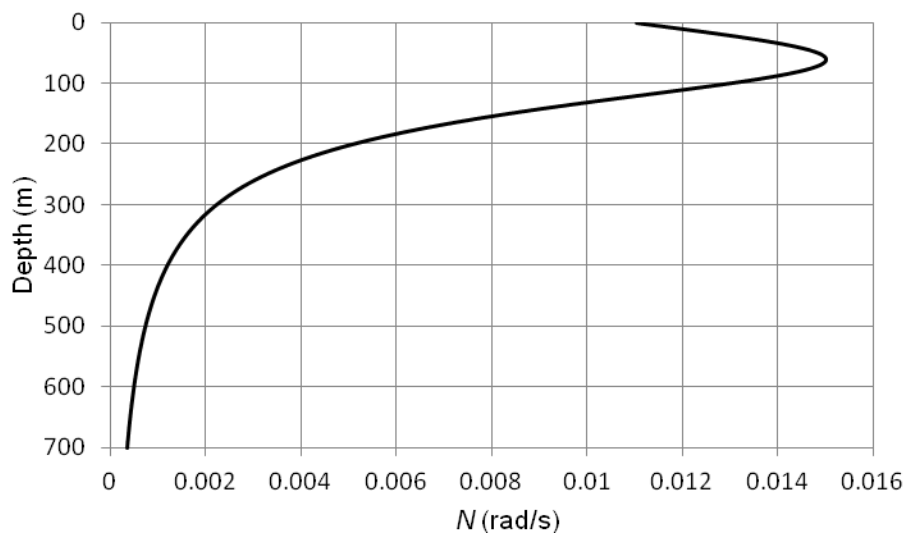

Figure 3. Gibraltar vertical profile.

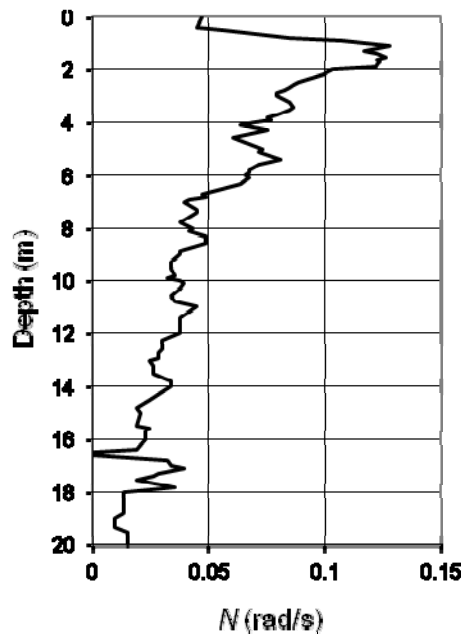

Figure 4. Loch Linnhe vertical profile.

Several other models are available from [10]. These can be represented approximately by a Lorentz distribution with the parameters in Table 1.

Table 1.
Internal Layer Parameters

Area	Peak *N* (rad/s)	Peak Depth (m)	Width (m)	Water Depth (m)	Mixed Depth (m)
Celtic Sea	0.015	30	50	200	0
Gulf of Mexico	0.045	15	20	275	5
New England Shelf	0.052	15	10	75	0
New York Bight	0.070	15	10	300	0
South West Africa	0.025	25	30	250	0
Sulu Sea	0.020	120	200	1800	0
US Pacific (N.W.)	0.090	6	6	30	2
Andaman Sea	0.023	100	150	1000	0

Hull Models

A number of hull models are available for the simulation. The primary models are the Taylor Standard Series, which are based on a British cruiser and are applicable to twin screwed warships [11], and the David Taylor Model Basin (DTMB) Series 60 models that are applicable to single screwed merchant ships [12]. In [3] it was demonstrated that, other than the principal dimensions, the most important hull parameter is the block coefficient, C_B, which represents the ratio of the volume of the submerged hull to the

volume of a rectangular parallelpiped that just encloses the submerged hull. While the Taylor model can be implemented over a continuous range of block coefficients, the DTMB model includes 5 separate hull designs covering a range $0.6 \leq C_B \leq 0.8$. Warships designed for speed are generally slender with a low coefficient but merchantmen generally lie at the upper end of the range.

Secondary models are the Wigley model [13] for which $C_B = 4/9$, a single source separated from a single sink (doublet) model and a single source.

The ship models are published as tables of hull offsets or transverse coordinates at various positions or "stations" along the length of the hull. The data points tend to be widely spaced and intermediate offsets and longitudinal positions must be interpolated; numerical splines are the preferred choice as this mimics the procedures that were formerly used in ship-building. The Taylor series is based on a parent form (a plan view from keel to waterline is shown in Figure 5) and an algorithm developed by Gertler allows its generalization into a series. Unfortunately some tables contain obvious typographical errors and in the Taylor Series there are some other minor errors needing correction [14]. Also the algorithm is only satisfactory for $0.5 \leq C_B \leq 0.7$. Outside this range, the hull forms become increasingly unrealistic.

A similar plot of a DTMB form using splines is shown in Figure 6. These plots demonstrate that spline interpolation is satisfactory.

Figures 7 to 9 show plots of the offsets. The bow section offsets are on the right hand side of the plot and the stern section offsets are on the left. "FP" and "AP" are the forward and aft perpendiculars respectively. "WL" stands for waterline. The waterline for the Taylor model corresponds to the horizontal line at about half the height of the plot. For the DTMB model, it lies at "1.00WL" and for the Wigley model it corresponds to the lower horizontal line. The numbers are labels for the longitudinal stations. It is worth noting the small bulbous bow on the Taylor series and its absence on the DTMB series. The submerged aft section on the Taylor series is narrower than on the DTMB series to accommodate and support twin screws. The Wigley hull is parabolic in the transverse and longitudinal directions but the draft is constant unlike a true canoe shape. The example in Figure 9 also has freeboard.

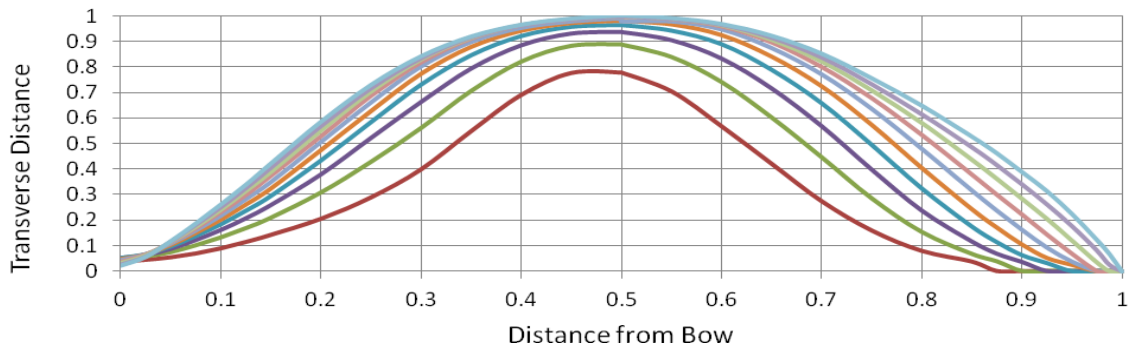

Figure 5. Plan view of Taylor parent hull offsets over 150 stations derived from original 29 stations using a cubic spline interpolation; $C_B \sim 0.493$. Red to light blue lines represent offsets at equal vertical intervals from close to keel to waterline.

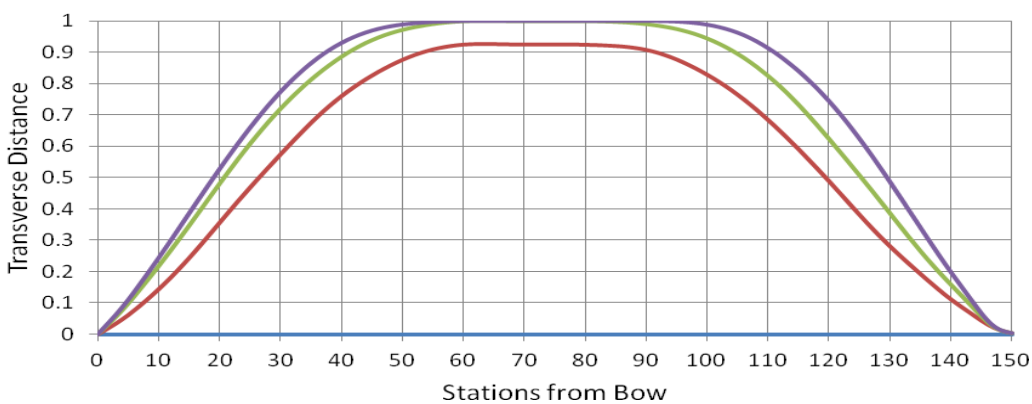

Figure 6. Plan view of DTMB Hull offsets over 150 stations derived from original 25 stations using a cubic spline interpolation; $C_B = 0.7$. Blue to purple lines represent offsets at equal intervals from keel to waterline.

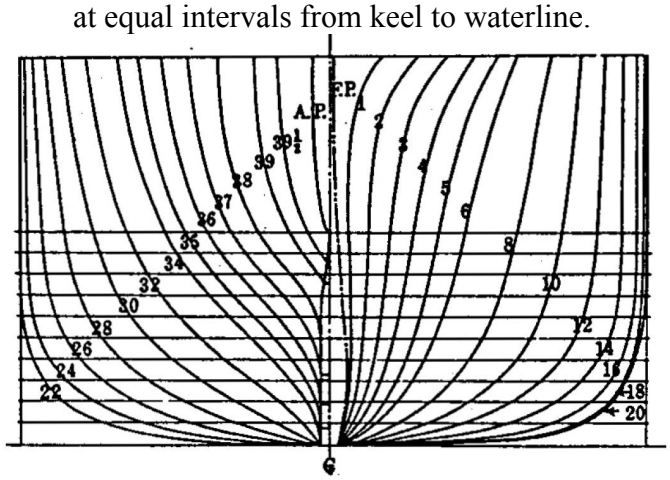

Figure 7. Example of Taylor series hull offsets (from [11]).

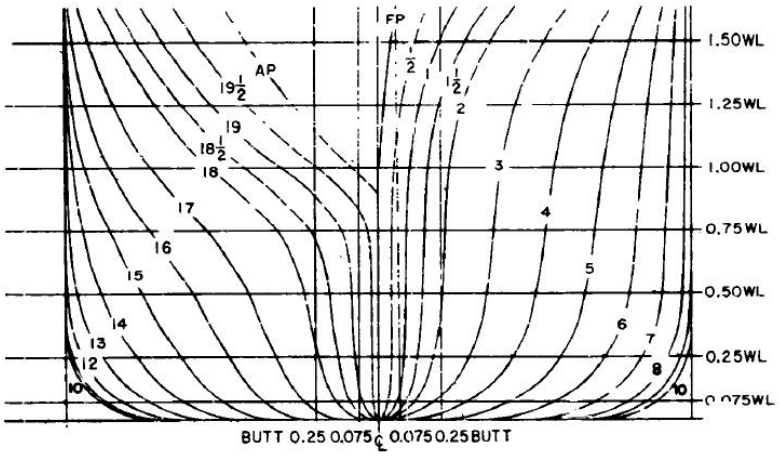

Figure 8. Example of DTMB Series 60 hull offsets for $C_B = 0.6$ (from [12]).

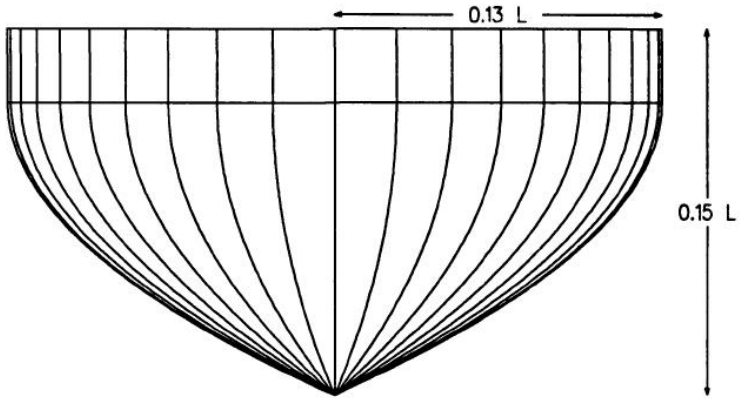

Figure 9. Example of Wigley hull offsets (from [13]).

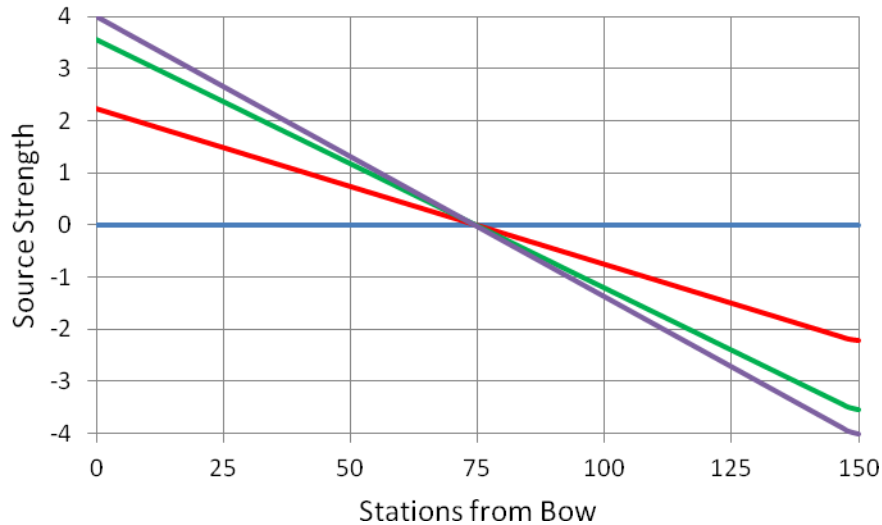

Figure 10. Source distribution for Wigley hull over 150 stations. The lines, blue to purple represent the distributions from the keel to the waterline at equal intervals of the vertical coordinate. The hull beam and length are one unit of length and the source strength is a volume per unit time.

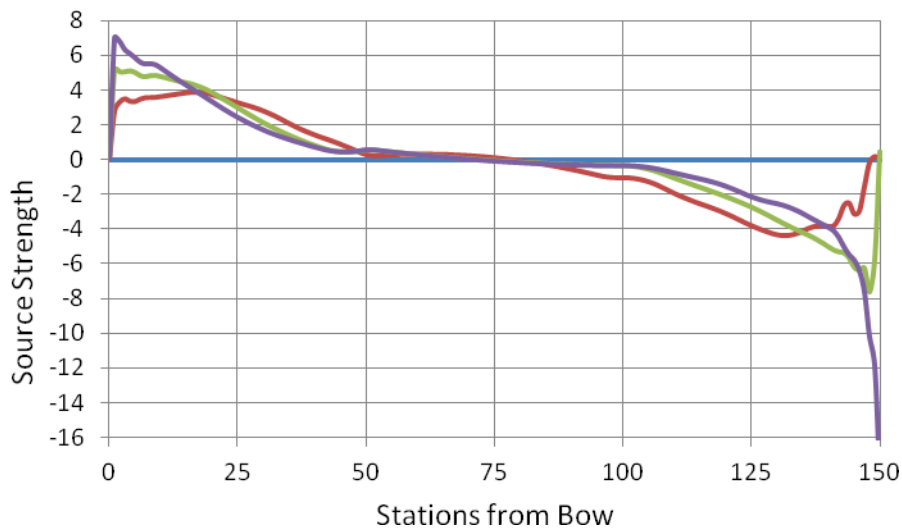

Figure 11. Source distribution for Taylor hull ($C_B = 0.7$) over 150 stations. The lines, blue to purple represent the distributions from the keel to the waterline at equal intervals of the vertical coordinate. The hull beam and length are one unit of length and the source strength is a volume per unit time.

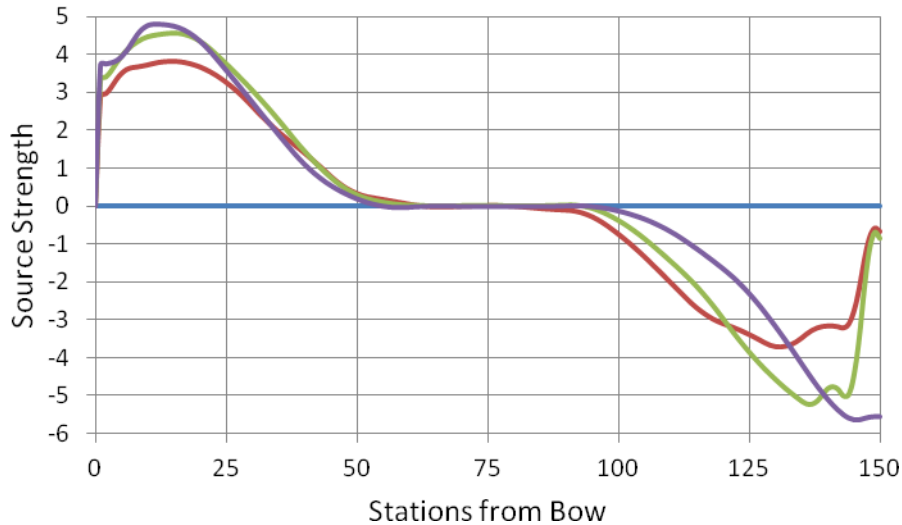

Figure 12. Source distribution for DTMB Series 60 hull ($C_B = 0.7$) over 150 stations. The lines, blue-red-green-purple, represent the distributions from the keel to the waterline at equal intervals of the vertical coordinate. The hull beam and length are one unit of length and the source strength is a volume per unit time.

Figures 10 to 12 show the source distribution curves for the Wigley, Taylor and DTMB Series 60 hulls. In the last two cases the block coefficient is 0.7. The distributions over 4 horizontal slices are shown at equal height intervals. While the distribution for the Wigley hull is quite simple, the distributions for the practical hulls are much more complicated. The bow and stern sections are separated and there is a distinct midships section where the distribution is close to zero. The distribution of the bow section reflects efforts to improve seakeeping and reduce deck-wetting as well as to reduce wave resistance; the stern distribution reflects the necessity of accommodating either twin screws and shafts or a single screw.

Theory

This is based on previous work [1] and a summary is as follows.

In principle, waves on the layer at a given depth are represented by a sum of horizontally propagating waves. The amplitudes of a wave as a function of depth are solutions of a differential equation subject to boundary conditions that must be solved numerically:

$$\frac{d^2 Q_z}{dz^2} + k^2\left(\frac{N^2(z)}{\omega^2} - 1\right)Q_z = 0 \qquad (1)$$

Here Q_z is the Fourier transform of the vertical flux, N is the B-V frequency, ω is the angular frequency and k is the angular wave number. The equation is sometimes known as the Taylor-Goldstein equation but in our case it is the simplest version because currents and current shears are neglected. The boundary conditions are simplified by neglecting the usual surface gravity waves but this has no practical effect on the solution because the vertical displacements due to internal waves are very small. The vertical fluid velocity is set to zero at the fluid surface as well as at its floor. Because wake waves exist

over a wide range of frequencies, the differential equation must be solved over this range. At each frequency, a solution of the equation yields a sequence of eigenvalues and eigenvectors. Each member of the sequence represents a mode of oscillation. An eigenvalue is the angular wave number of the horizontal wave and the corresponding eigenvector is its normalized amplitude as a function of depth. In principle, the final amplitude is a sum over these eigenvectors; the coefficients would depend on how the waves are generated.

The Taylor-Goldstein equation is of the Sturm-Liouville type. However, the weighting factor, conventionally denoted by ρ, is not always positive as is usually assumed in standard texts, such as [15] or [16]. (The situation is further confused by the omission of the factor ρ in an equation at the top of page 295 in [15].) This is because the application is usually to waves on non-homogeneous strings where the solutions are always oscillatory. In the present application to internal waves, the waves are constrained within the layer and tend to fall off exponentially above and below it; in these regions ρ is negative. Therefore it seems prudent to confirm that the usual theory is applicable. The theory is discussed in Appendix 1, where it is shown that the only potential problem is a failure to normalize the eigenvector at some frequencies. It is worth noting that so far this has never occurred numerically and it may reasonably be concluded that the usual Sturm-Liouville theory is satisfactory.

The lowest mode of oscillation is a sinuous mode in which the entire layer moves up and down with amplitudes that depend on depth and are proportional to a sum of the eigenvectors of this lowest mode. Clearly these eigenvectors have no zero-crossings. If a vessel is above or below the layer peak, as it moves horizontally, it tends to push the layer down or up and the lowest mode will predominate.

When a vessel is close to the peak of the layer, it tends to push the layer more or less equally in both directions. This corresponds to a varicose mode in which the propagating waves cause the layer to vary in thickness. This corresponds to the next lowest mode and its eigenvectors have a single zero-crossing. It turns out that the propagation velocities of the waves decrease rapidly as the mode number increases so that the lowest mode contributes the broadest wake and is the most important by far; higher modes can usually be neglected. The next mode is important only when a vessel is traveling close to the layer peak. This situation is not considered in detail here.

The relation between the frequency and the horizontal wave number in a given mode represents a dispersion relation. This is conveniently calculated by solving the Taylor-Goldstein equation at equal intervals of the wave frequency up to the maximum B-V frequency. The wave number at intermediate frequencies can be found by linear interpolation. As described in Appendix 2, the dispersion equation can be employed to find the crest pattern in the vessel wake. The crest pattern for any mode does not depend on the depth of the source generating the waves though this does affect the amplitude of waves in a wake [1]. The dispersion relation for the Gibraltar profile is shown in Fig. 13.

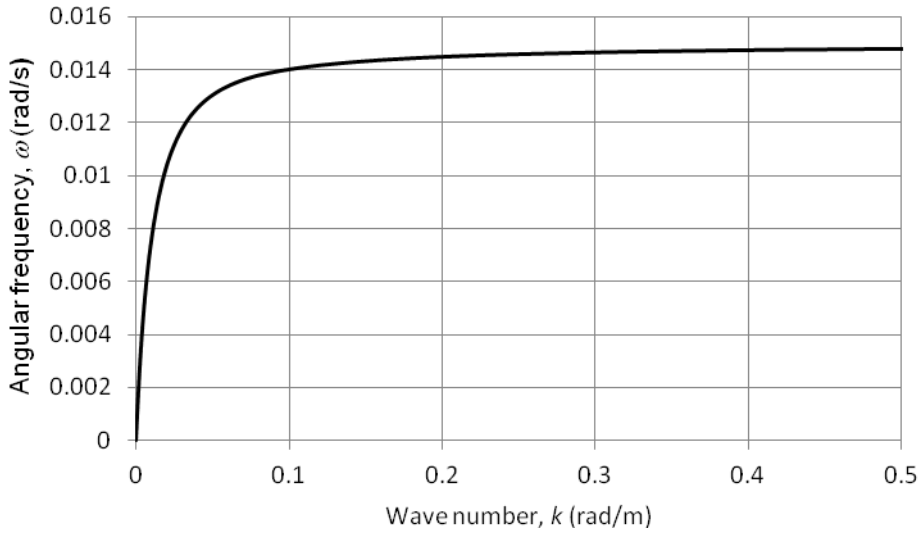

Figure 13. Dispersion relation of the lowest mode for the Gibraltar profile.

At very low wave numbers, the graph is linear and its slope is equal to both the group and phase velocities. As expected, the maximum frequency is equal to the maximum B-V frequency. Dispersion relations for all reasonable profiles have similar characteristics and resemble this. The dispersion relation for the Loch Linnhe profile is provided in Fig. 14. The graph exhibits some additional minor structure (at about 2.0 rad/m) associated with the complex structure in the original profile.

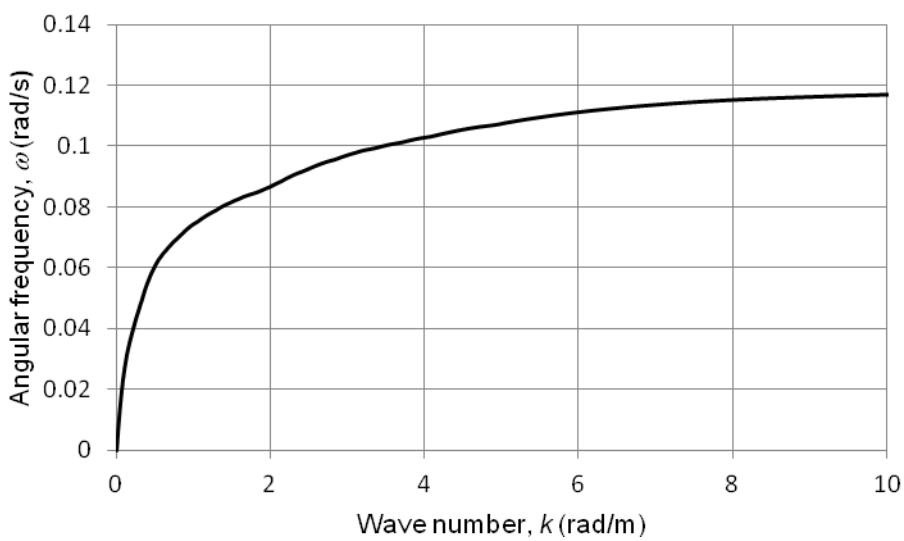

Figure 14. Dispersion relation of the lowest mode for the Loch Linnhe profile.

The eigenfunctions, which depend on frequency, represent the variation of amplitude of a mode at a given frequency. At low frequencies they are easily found during the solution of the Taylor-Goldstein equation. At high frequencies, close to the maximum B-V

frequency, numerical problems can occur and these are discussed later. Examples are shown for the first two modes at intermediate frequencies in each of the two layer profiles in Figs. 15 to 18.

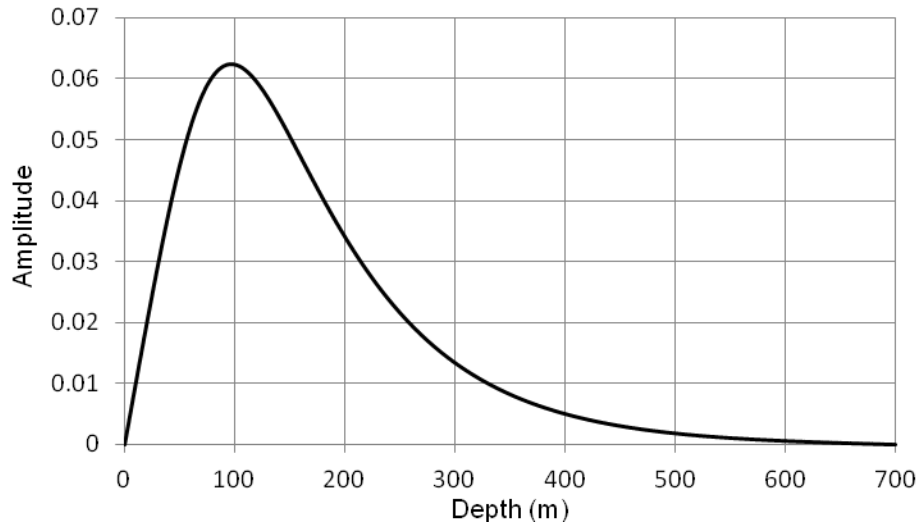

Figure 15. Eigenfunction for lowest mode of Gibraltar profile for frequency of 0.0075 rad/s. The amplitude, which is in arbitrary units, is proportional to the vertical flux.

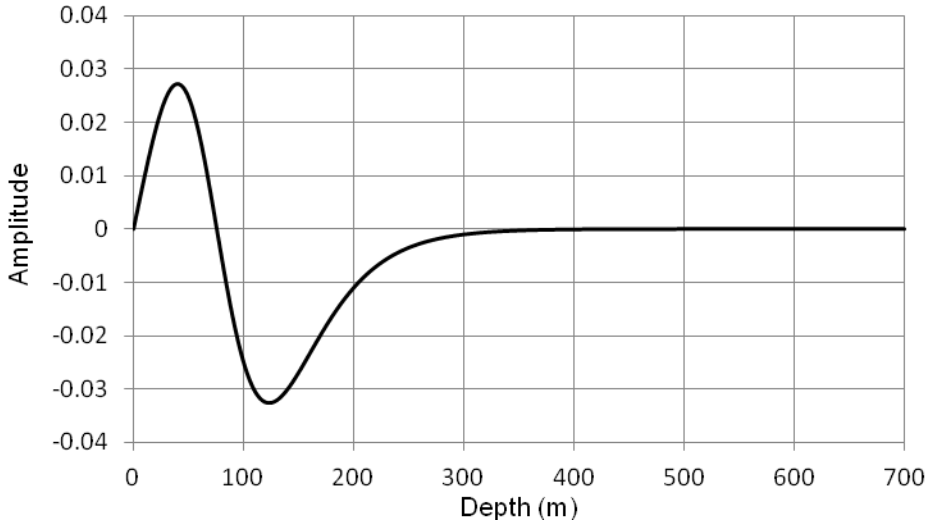

Figure 16. Eigenfunction for next lowest mode of Gibraltar profile for frequency of 0.0075 rad/s.

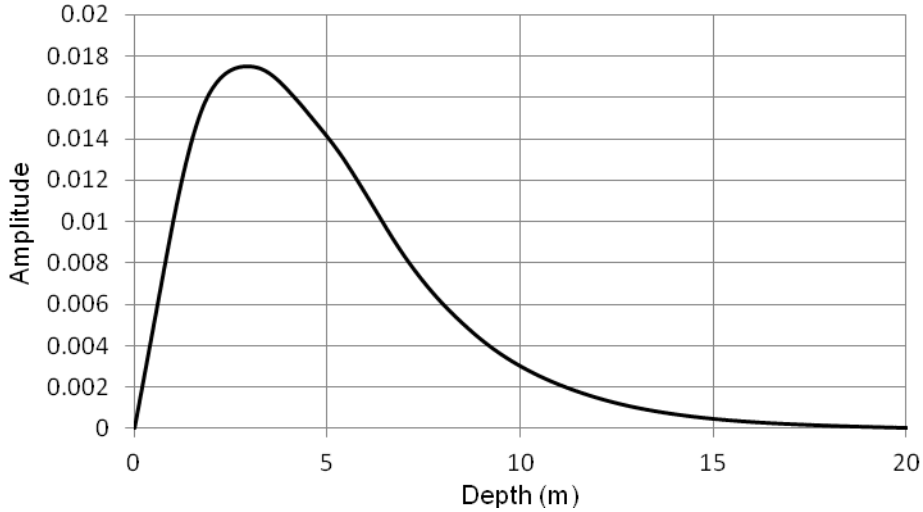

Figure 17. Eigenfunction for lowest mode of Loch Linnhe profile for frequency of 0.0625 rad/s.

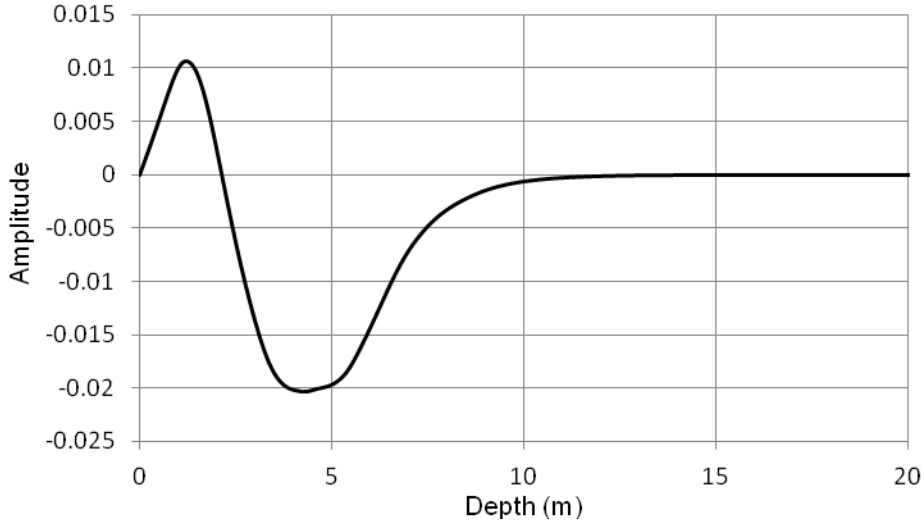

Figure 18. Eigenfunction for next lowest mode of Loch Linnhe profile for frequency of 0.0625 rad/s.

In the lowest mode the low-frequency eigenfunctions seem to be a smoothed version of the B-V profile. At higher frequencies, ω, close to the maximum B-V frequency, eigenfunctions peak strongly when the B-V frequency, $N > \omega$. The Loch Linnhe profile exhibits two peaks here and indeed there can be two smoothed peaks in the eigenfunction.

Waves in a wake are produced as the vessel creates a disturbance in the water during its movement, which for our purposes is a constant horizontal velocity. Waves propagate

outwards from their point of creation at the group velocity. At a given point in the wake, which is stationary in the reference frame of the vessel, waves interfere constructively so that a phase condition must be met. This is equivalent to insisting that the component of the vessel velocity in the direction of the wave must be equal to the phase velocity of the wave. If the phase of the wave is defined to be zero at the ship, the first crest occurs when the phase is 2π, etc. Using the dispersion curve, such as that in Figure 14, these concepts can be combined and are sufficient to calculate the crest pattern. The method is described in Appendix 2, where it is shown that the locus of a crest is determined in terms of the phase and group velocities and how they vary with frequency.

For example, the pattern for the first 5 crests is shown in Figure 19 for a ship traveling at 2 m/s over the profile in Figure 4. This can be compared to the image of a wake from the Loch Linnhe trials in Figure 1. The pattern is a good match to the radar observations. The crest pattern for the next mode is similar except that the wake is much narrower.

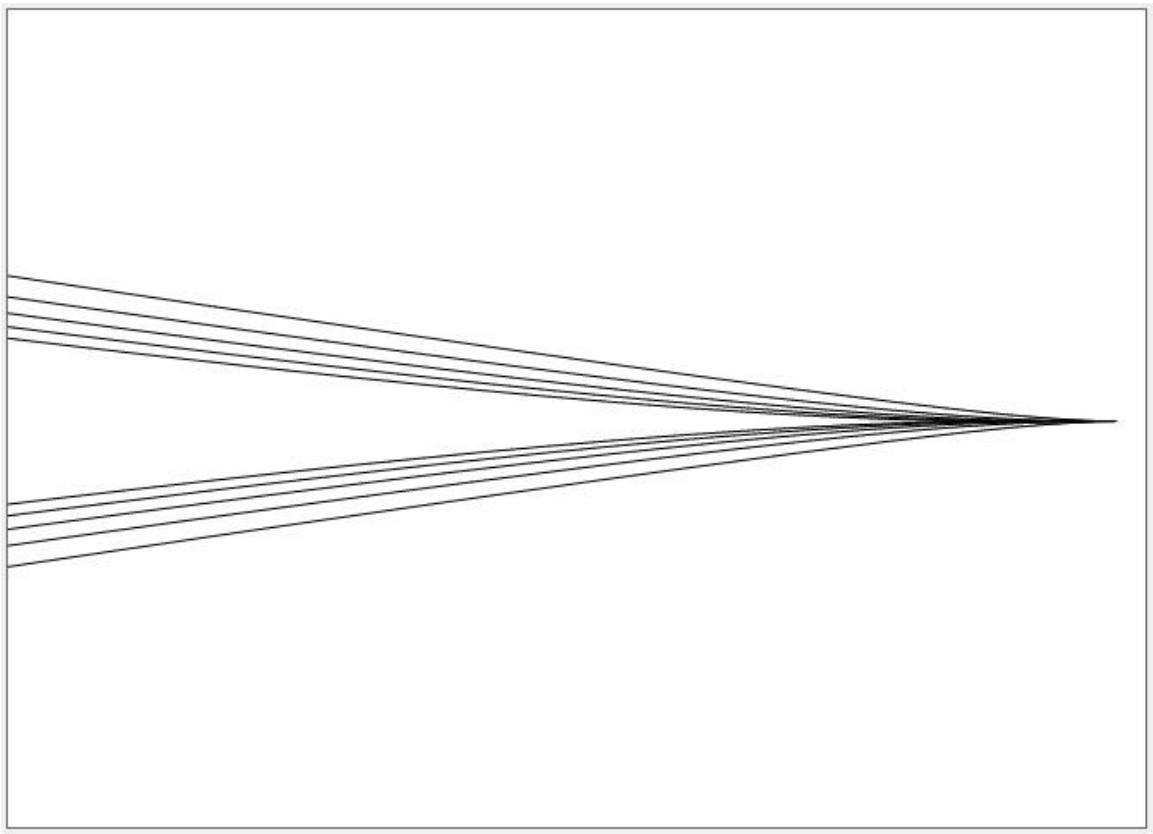

Figure 19. The lowest mode crest pattern for the Loch Linnhe profile showing the first 5 crests, which are the most prominent. The ship speed is 2 m/s and the image length is 4 km. The ship is located at the right hand edge of the picture box.

In [1] the theory was sketched and (inserting the correct coefficient for the inverse transforms) it can be shown that the vertical component of the flux, q_z, for a stationary oscillating source at depth c is given by:

$$q_z = -\frac{1}{(2\pi)^3}\int\sum_n \frac{Q_n(z)\delta(\omega-\omega_0)}{k_n^2-k^2} S_0\left(\frac{\partial F_n}{\partial z}\right)_{z=c} e^{i(\omega t-\mathbf{k}.\mathbf{r})} d\mathbf{k}d\omega \tag{2}$$

Here, z is the vertical coordinate (positive downwards), k_n and Q_n are the eigenvalue and the orthonormal eigenvector for mode n; ω and $\mathbf{k}$ are the wave frequency and wave vector, respectively. The source strength is S_0 and this can be expressed as a mass of fluid per unit time. The function F_n is given by:

$$F_n = Q_n(z)\left(\frac{N^2(z)}{\omega^2}-1\right) \tag{3}$$

where N is the B-V frequency. If we are only interested in the lowest mode, which we label '0', and perform the integral over frequency, we have:

$$q_z = -\frac{1}{(2\pi)^3}\int \frac{Q_0(z)}{k_0^2-k^2} S_0\left(\frac{\partial F_0}{\partial z}\right)_{z=c} e^{i(\omega_0 t-\mathbf{k}.\mathbf{r})} d\mathbf{k} \tag{4}$$

We now shift the frame of reference from the fluid to a constant source moving at velocity $\mathbf{U}$ and combine this with the Doppler equation, which is:

$$0 = \omega_0 - \mathbf{k}\cdot\mathbf{U} \tag{5}$$

Then we have for the wake:

$$q_z(\mathbf{r}') = -\frac{1}{(2\pi)^3}\int \frac{Q_0(z)}{k_0^2-k^2} S_0\left(\frac{\partial F_0}{\partial z}\right)_{z=c} e^{-i\mathbf{k}.\mathbf{r}'} d\mathbf{k} \tag{6}$$

where

$$\mathbf{r}' = \mathbf{r} - \mathbf{U}t \tag{7}$$

Clearly $\mathbf{r}'$ is the position of a point in the wake relative to the source. A dimensional analysis can be implemented using Table 2 (this includes variables used in [1]); it is easily verified that (6) is dimensionally correct.

Table 2.
Variable Dimensions

Variable	Dimensions
q	$M/(L^2T)$
k	$1/L$
$d\mathbf{k}$	$1/L^2$
ω	$1/T$
S	$M/(L^3T)$
S_0	M/T
Q	M
Q_n	$1/L^{1/2}$

As shown in Appendix 2, at each point in the wake a wave of specific frequency and wave number predominates. The values of these parameters can be established geometrically. This would allow the integral in (6) to be evaluated by determining the value of k_0 at a point. The phase of the wave is also determined.

Appendix 3 provides the details of the determination of the horizontal surface flow and the evaluation of the integral using the stationary phase method. The horizontal flow is related to q_z by the fact that the divergence of the velocity is zero (water is incompressible). The limits of integration for k can be extended over [-∞, ∞] because waves in the far wake must propagate at an angle θ to the ship's track and cannot propagate in the reverse direction. They can also be considered to be slightly damped to establish that the pole that contributes to the integral in a contour integration lies in the upper half of the complex plane. The remaining integral over θ is evaluated by a stationary phase technique as was employed by Tunaley [17]. Subsequently Chunchuzov et al. [18] appear to have used a similar approach.

Appendix 5 provides some comparisons between the discrete and diffuse theories and confirms consistencies between the two approaches.

Numerical Analysis

The first part of the simulation is the calculation of the eigenvalues and eigenvectors of the Taylor-Goldstein equation. The eigenvalue represents the wave number of horizontally propagating waves and its eigenvector represents the amplitude of the vertical component of the mass flux as a function of depth. This calculation must be completed for a range of frequencies.

The amplitude of the vertical component of the mass flux (fluid density times the velocity) is zero at the surface but its derivative with depth here can be given a small positive value. If some arbitrary value is assigned to the horizontal wave number, the differential equation can then be marched forward. Typically, the amplitude will increase with depth as the maximum B-V frequency is reached and then it will either increase or decrease rapidly reaching large positive or negative values at the bottom of the fluid. The desired solution is the value of the wave number when the amplitude at the bottom is zero.

One way to achieve this is to perform the integration using the Runge-Kutta (R-K) algorithm. Implicit in this is the idea that the B-V frequency is reasonably smooth. This algorithm appears to function successfully at frequencies up to about ¾ of the maximum B-V frequency and delivers reasonable eigenvalues and eigenvectors but then several problems start to emerge. These involve the precision of the floating point numbers and the accuracy of the R-K algorithm.

The eigenvalue can be established using a bisection search to locate the appropriate horizontal wave number to make the amplitude at the bottom zero. As the frequency increases beyond a critical fraction of the B-V frequency, the sensitivity of this amplitude grows to such an extent that double precision is wholly insufficient to locate the eigenvalue such that the eigenvector is satisfactory. Therefore an eigenvalue can be obtained accurately but the eigenvector may exhibit a sharp upturn or downturn of large amplitude near the ocean bottom. In extreme cases, the eigenvector is useless. Even though the code is in C-Sharp, which is very forgiving of floating point overflow, "Not a Number" (NaN) was returned for some calculations. In part, these effects may be

attributed to small errors introduced by the R-K algorithm itself. Therefore the R-K algorithm was replaced by a matrix approach, which is described in Appendix 4.

Unlike the R-K model, the model of the layer in the matrix approach is stepwise in nature, so that the B-V frequency can change discretely from step to step but is constant over each step. The solution of the Taylor-Goldstein equation is either sinusoidal (if the frequency is less than the local BV frequency) or exponential (if it is greater). Any second order differential equation can be replaced by two single order differential equations so that a marching solution can be expressed as a matrix multiplication with a two-component vector. The vector components are typically the amplitude and its derivative (see Appendix 4). Therefore, subject only to rounding errors and the limitations of the stepwise model, the integration can be performed exactly.

When this model was implemented, the problems of the limited precision and the sensitivity of the eigenvector to the eigenvalue remained. However, by limiting the magnitude of the variables, the NaN returns can be eliminated and the upturns or downturns can simply be set to zero (or just ignored). This provides satisfactory eigenvectors over the entire range of frequencies and wave numbers that are required.

The present algorithm functions well for the Loch Linnhe and Gibraltar profiles and yields close but not exactly similar eigenvalues and eigenvectors to those using the R-K approach. Small discrepancies, such as those observed, are expected because the models are not identical.

While the development was principally for the lowest mode, the algorithm was tested for the second mode, which has a single zero-crossing. It functions well for this mode too.

The Program

The program was constructed using Microsoft's Visual Studio in the C-Sharp language. The main window is shown in Figure 20. The B-V profile can be loaded from a file or be created using a Lorentzian model by clicking on the appropriate radio button. In the latter case the B-V frequency is finite at the surface and there is no mixed layer, which is similar to the standard Loch Linnhe profile.

The operator must also specify the length of the wake to display and an offset for the velocity profile along a track that is parallel to the wake axis.

There is a choice of hull type using radio buttons and the vessel's principal dimensions can be entered. The "Go" button is then clicked. If the hull model is a Taylor or DTMB type, a subsidiary window allows the operator to choose a block coefficient within limits or from a list, respectively. When the hull is a single source, a doublet or submarine, a subsidiary window allows the operator to enter a depth. The source strengths for these are calculated from the vessel's draft, T, and beam, B, using an elliptical transverse profile model. Thus the source strength, $S_0 = \pi BTU/4$ (U is the source speed). The separation of the doublet (a source of strength S_0 and an equal and opposite sink) is set to the vessel's length, L.

The output is a display of the surface velocity component transverse to the axis of the wake. Beneath this is a graph of the transverse velocity component along a track that is parallel to the wake axis and offset from it by the specified distance. The time on a typical personal computer running Microsoft's Windows operating system is usually less than 20 s.

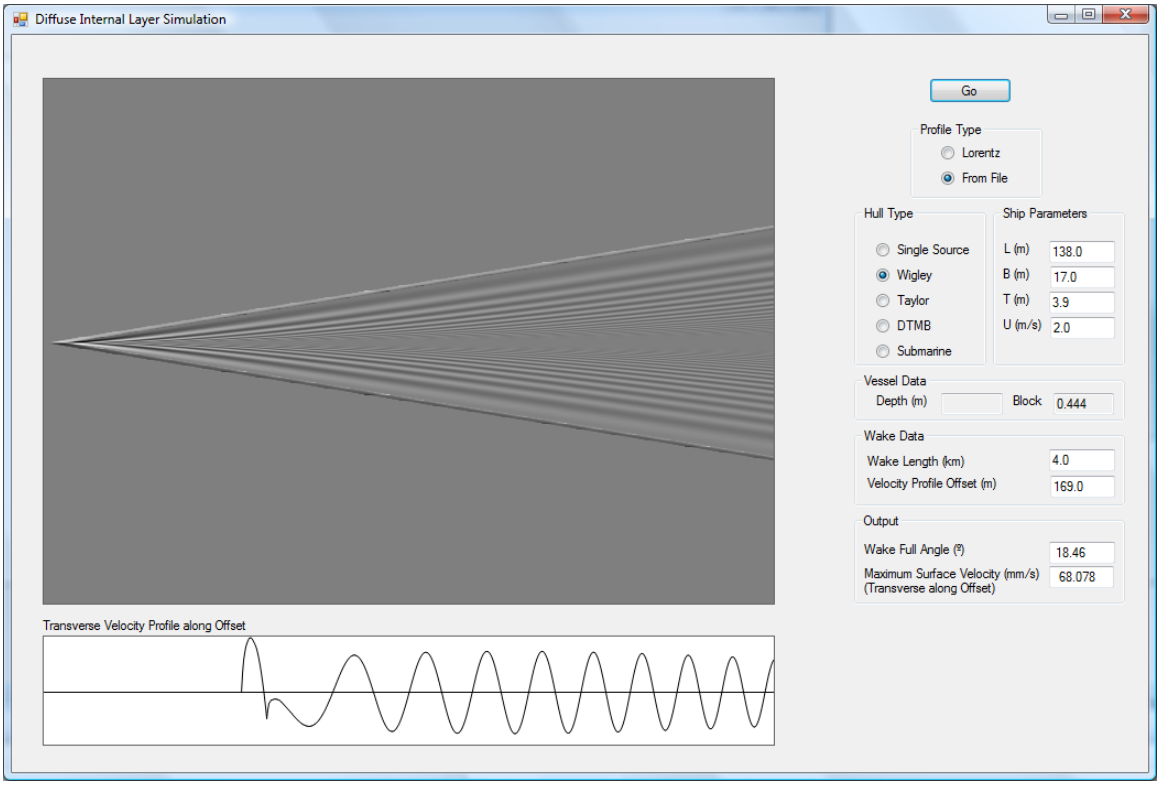

Figure 20. Main window of simulation program.

The example in Figure 20 is for the Loch Linnhe B-V profile and the Sir Tristram ship. The hull type is Wigley. Differences in the appearance of the wake in the main display do occur when the ship hull is changed to a Taylor or DTMB model and when the block coefficient is changed. However, these are quite minor and are not easily discerned. However, they are usually quite obvious in the graph beneath.

The full wake angle and the maximum transverse velocity along the offset track are also output.

Simulation Results

To verify the current simulation of a diffuse layer and also the previous simulation using a discrete layer, simulations were compared to each other and to the Loch Linnhe trials data. Figure 21 shows an example of the transverse wake surface velocity component that was derived from observational data for a wake generated by the Sir Tristram landing

ship. These data were band-passed filtered to reduce the noise components. The effectiveness of this and the magnitude of the errors are not clear.

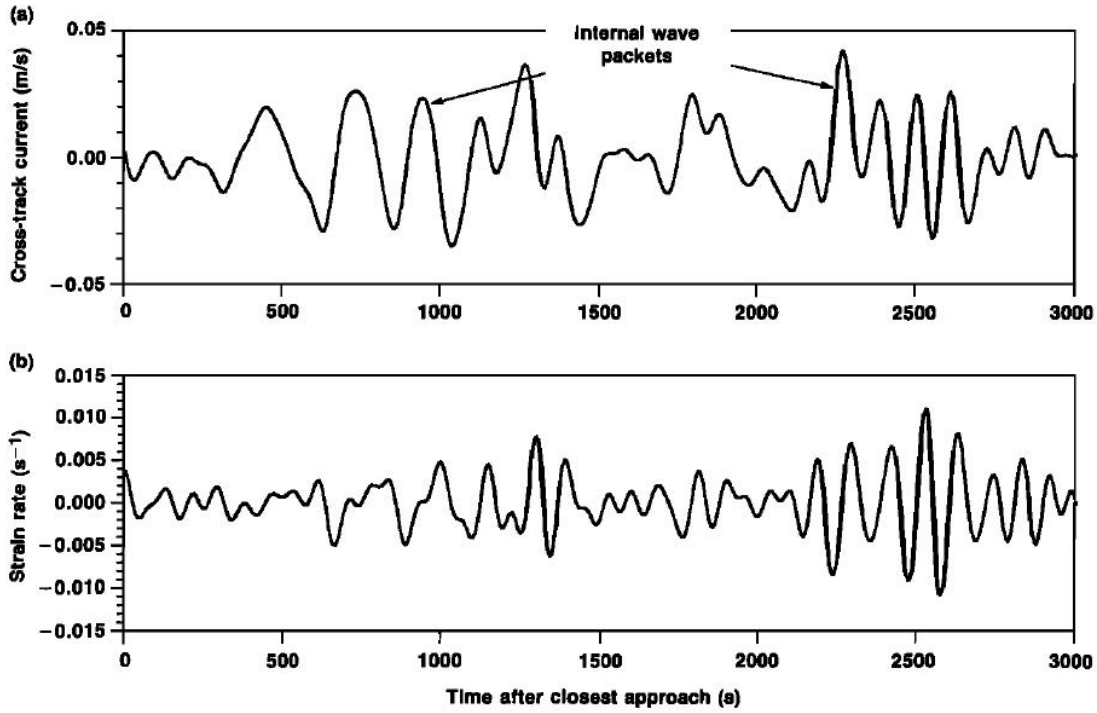

Figure 21. Measured cross-track current (and strain rate) corresponding to Sir Tristram simulation, $U = 2.0$ m/s (from [5]).

Figure 22 shows a simulated version assuming the depth of a discrete layer was 3 m. The number of oscillations is too large compared with the observations but their amplitudes appear to have the appropriate magnitude. If the depth of the layer is increased to 5 m, the number of oscillations is reduced but their amplitudes are too small.

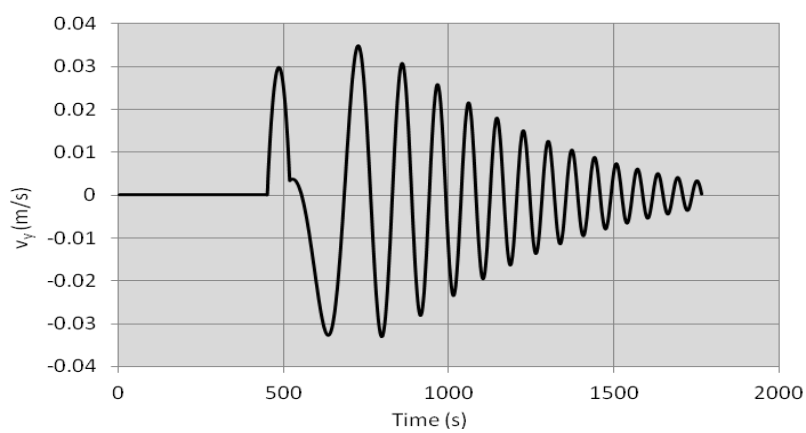

Figure 22. Simulated cross-track surface velocity component using a Wigley hull and depth of discrete interface of 3 m (from [3]).

The corresponding velocity profile for the Sir Tristram simulation is shown in Figure 23, which is similar in part to the graph in Figure 20. The B-V profile in Figure 4 was employed and it was assumed that the Sir Tristram had a length of 138 m, a beam of 17 m and a draft of 3.9 m [3]; its speed was 2 m/s. The resolution in depth for the simulation was 0.1 m and the horizontal resolution was about 6 m. The horizontal axis is in distance rather than time (as in Figure 21); the conversion involves just a factor of 2. The number of oscillations is of the correct order and apparently the amplitude is greater than that observed by about 30%. In addition, the general shape of the profile is similar to that of the discrete simulation including the irregularity or shoulder at about 1200 m. The agreement suggests that the simulation is providing reasonable results and that, unlike the discrete layer model, no corrections are needed to achieve approximate agreement simultaneously between the amplitudes and the number of oscillations.

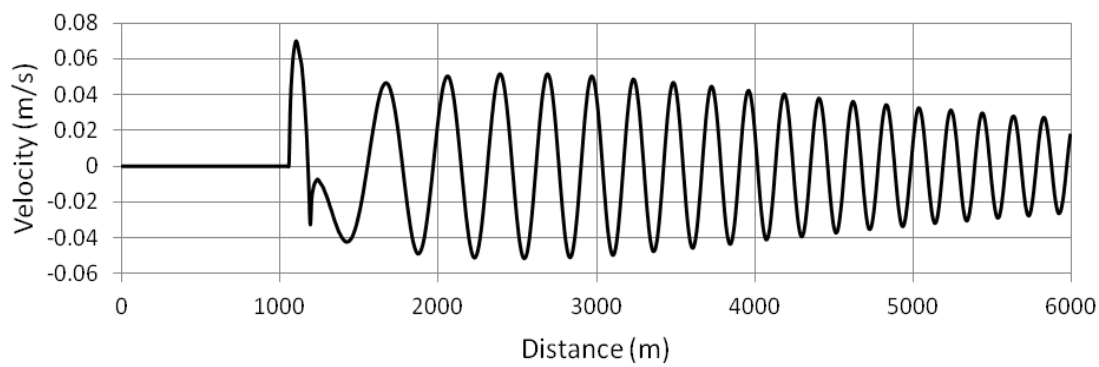

Figure 23. Simulation of velocity profile 169 m from ship track using diffuse layer and Wigley hull.

The effect of changing the hull design to a Taylor or a DTMB Series 60 type is shown in Figures 24 to 27.

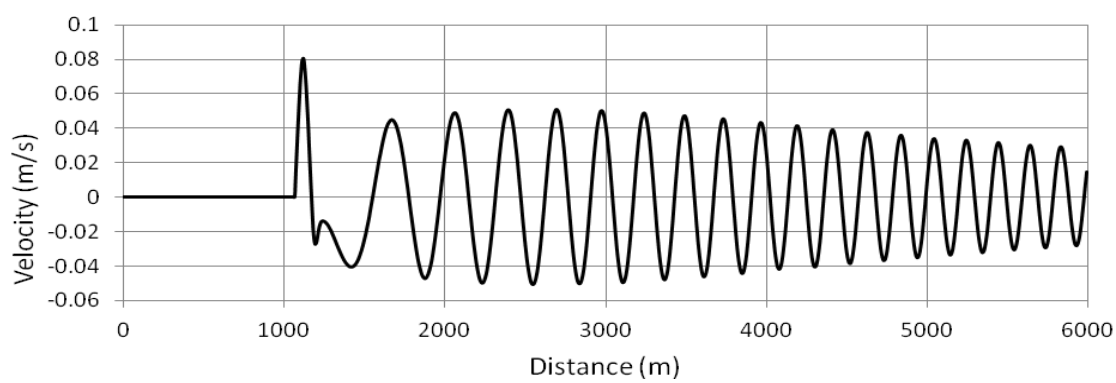

Figure 24. Simulated velocity profile using the previous parameters with a Taylor hull with block coefficient, C_B, of 0.5.

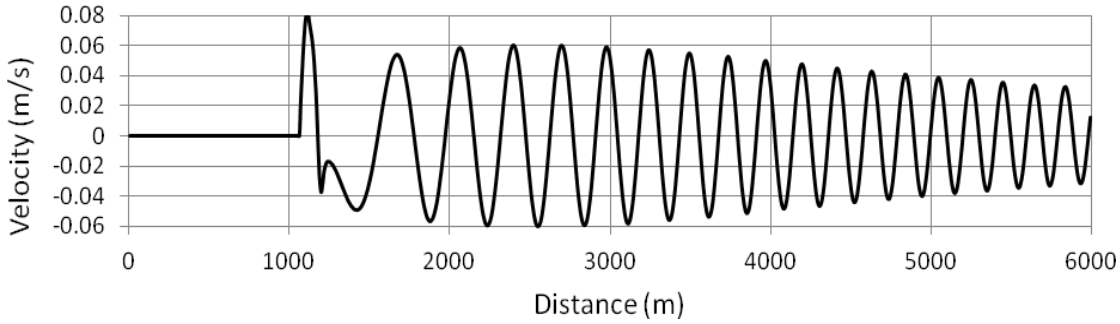

Figure 25. Simulated velocity profile using the previous parameters with a DTMB Series 60 hull with block coefficient, C_B, of 0.6.

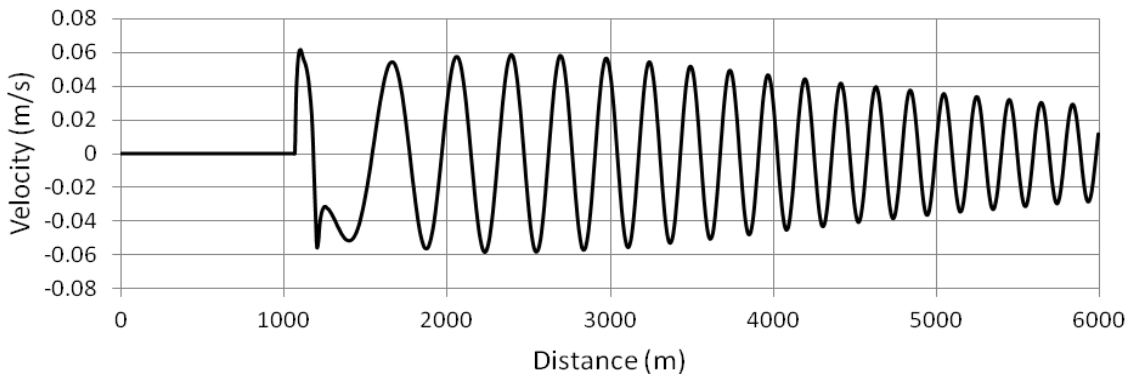

Figure 26. Simulated velocity profile using the previous parameters with a Taylor hull with block coefficient, C_B, of 0. 7.

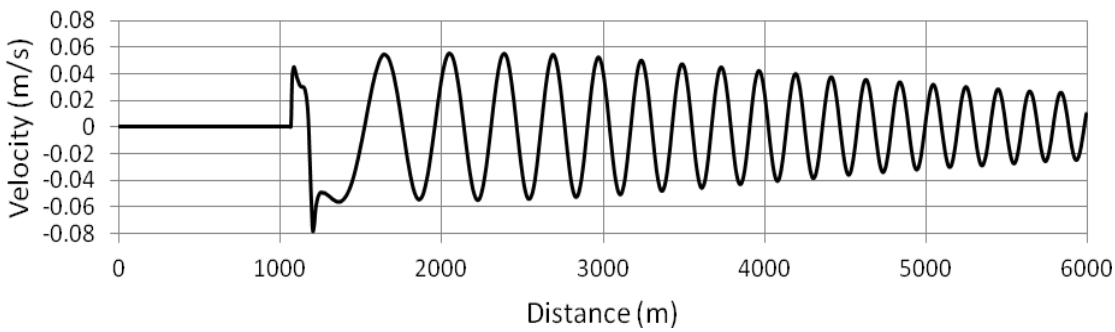

Figure 27. Simulated velocity profile using the previous parameters with a DTMB Series 60 hull with block coefficient, C_B, of 0.8.

As with the discrete layer, the main differences associated with the hull are in the leading cycles of the velocity profiles. These change shape and the shoulder tends to become more pronounced as the block coefficient rises. Otherwise the amplitudes of the surface velocities remain much the same.

A plot of the maximum transverse surface flow velocity along the parallel track against ship speed is shown in Figure 28 for the Sir Tristram. The layer profile is appropriate to

the Loch Linnhe trials and the Taylor model was used with a block coefficient of 0.7. When the ship speed is greater than about 2.5 m/s, the maximum transverse flow velocity barely changes. As the ship speed increases, the decrease in flow velocity is due to the additional distance of the sensor from the ship as it encounters the wake. The general result seems to be in accord with remarks in [5], in which it is noted that the maximum observed flow velocities from the Sir Tristram are always about 3 cm/s .

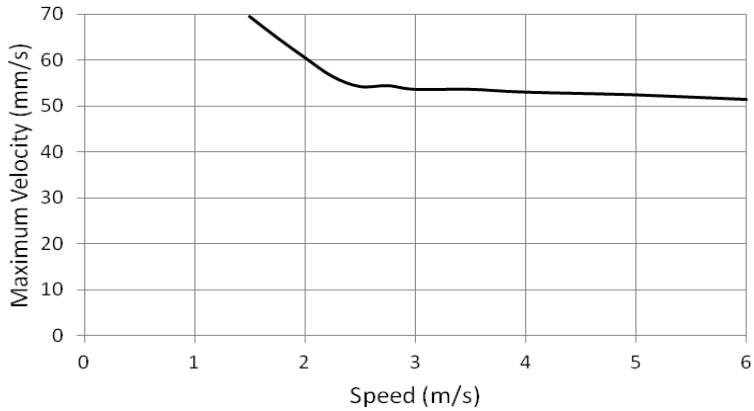

Figure 28. Variation of maximum surface velocity with ship speed.

A mixed layer has a profound effect on the amplitudes of the internal wave wake. The main widow for a simulation with a mixed layer 4 m deep above the standard Loch Linnhe profile is shown in Figure 29; the hull is of the Wigley type. The B-V frequency is zero in this mixed layer. The Sir Tristram draft is similar to the layer depth so that the ship does not penetrate the layer where the B-V frequency is finite. There are several obvious effects. Firstly, the maximum amplitude of the surface velocity along the parallel track is much smaller than in the absence of a mixed layer. Secondly, the polarity of the surface velocity is reversed because all sources over the ship are now pushing the layer downwards rather than the previous net effect of an upwards push. Thirdly, the wake angle has increased.

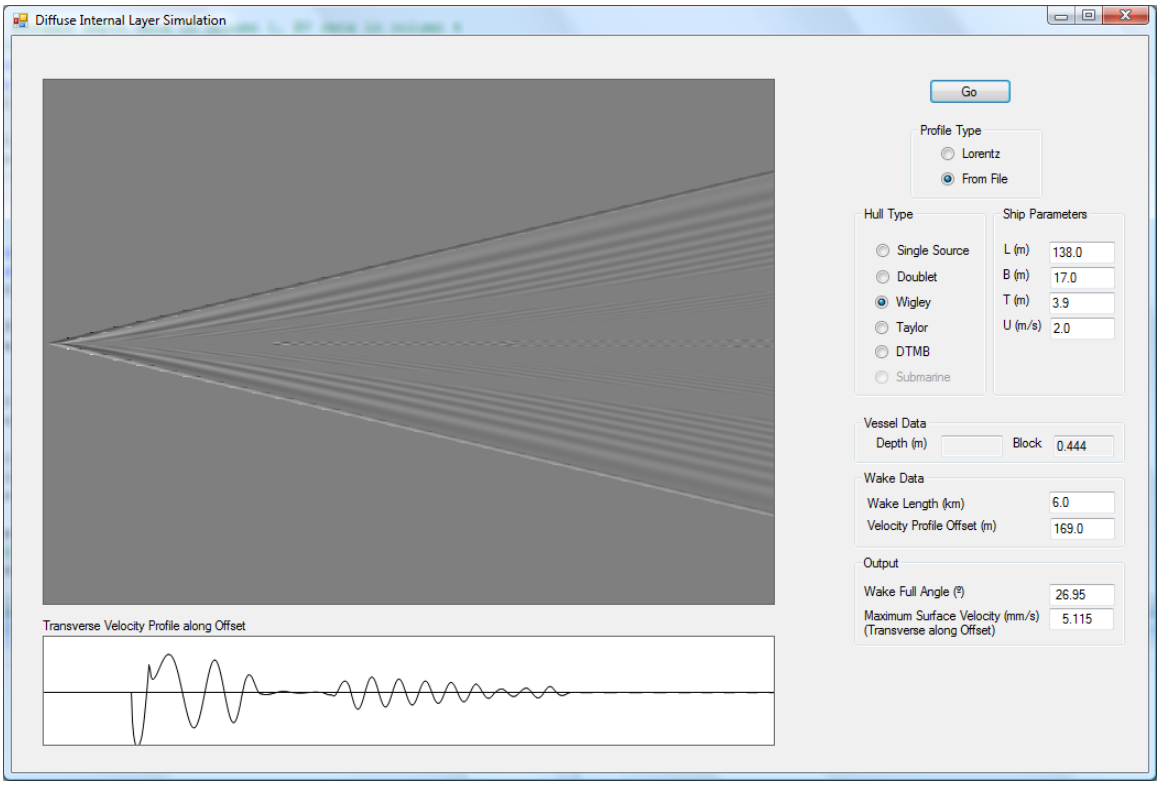

Figure 29. Main window of the simulation using the Sir Tristram ship with a 4 m mixed layer above the standard Loch Linnhe profile.

The velocity profile for the above simulation is plotted in detail in Figure 30. This profile is more complicated than those considered previously mainly because there is now significant interference between sources at the bow and sinks at the stern. The maximum transverse surface velocity along the parallel track is about 5 mm/s compared with velocities of 30 mm/s during the Loch Linnhe trials. This suggests that the presence of the mixed layer probably renders the wake undetectable by SAR using current technology.

If the mixed layer thickness is increased by one additional meter, the result is shown in Figure 31. The surface velocity amplitudes are reduced by a factor of approximately two. This demonstrates that mixed layers above the main internal layer have a very negative effect on wake detectability at the surface. The wake angle is increased to about 28º.

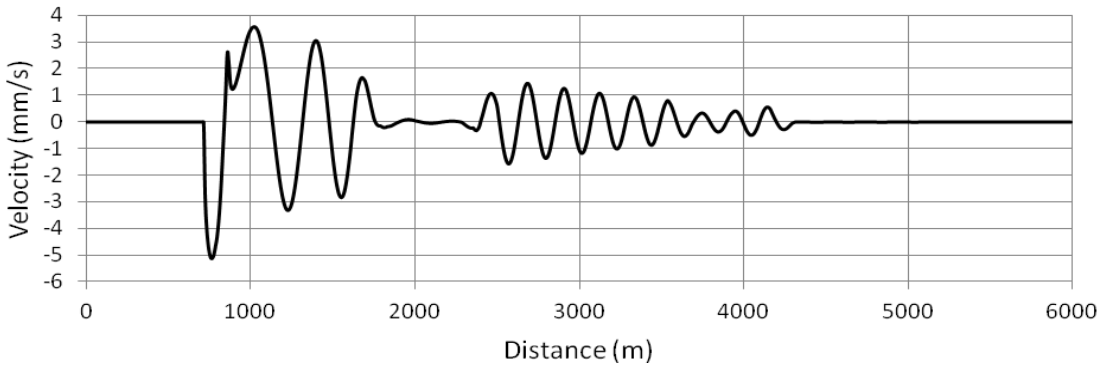

Figure 30. The velocity profile showing the effect of a 4 m thick mixed layer.

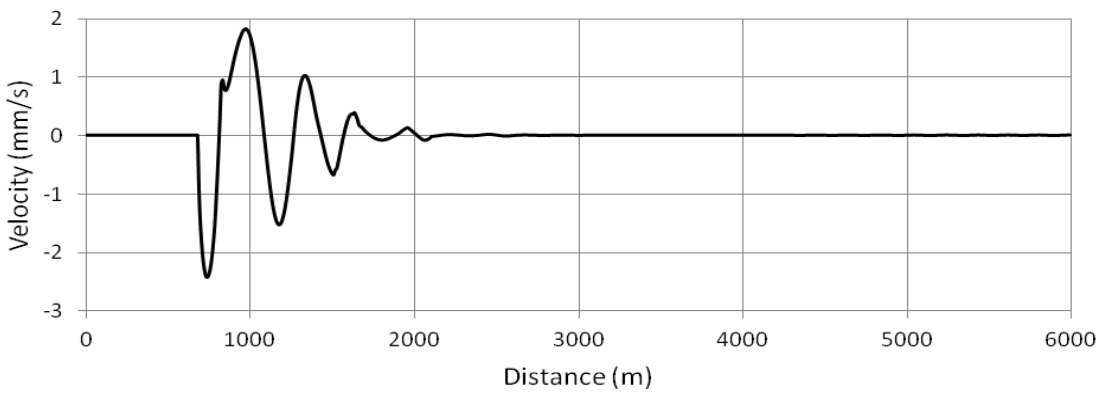

Figure 31. The velocity profile showing the effect of a 5 m thick mixed layer.

An example of a simulation main window with the Gibraltar layer profile and a Wigley hull representing the Sir Tristram moving at 5 m/s is shown in Figure 32. The wake comprises a 'V' with virtually no visible internal structure. The maximum surface velocity amplitude along the parallel track is a fraction of a millimeter per second. As the speed of the ship increases, the amplitude increases but quite slowly, so that the wake might not be detectable even at much higher speeds. Details of the velocity along the parallel track are shown in Figure 33.

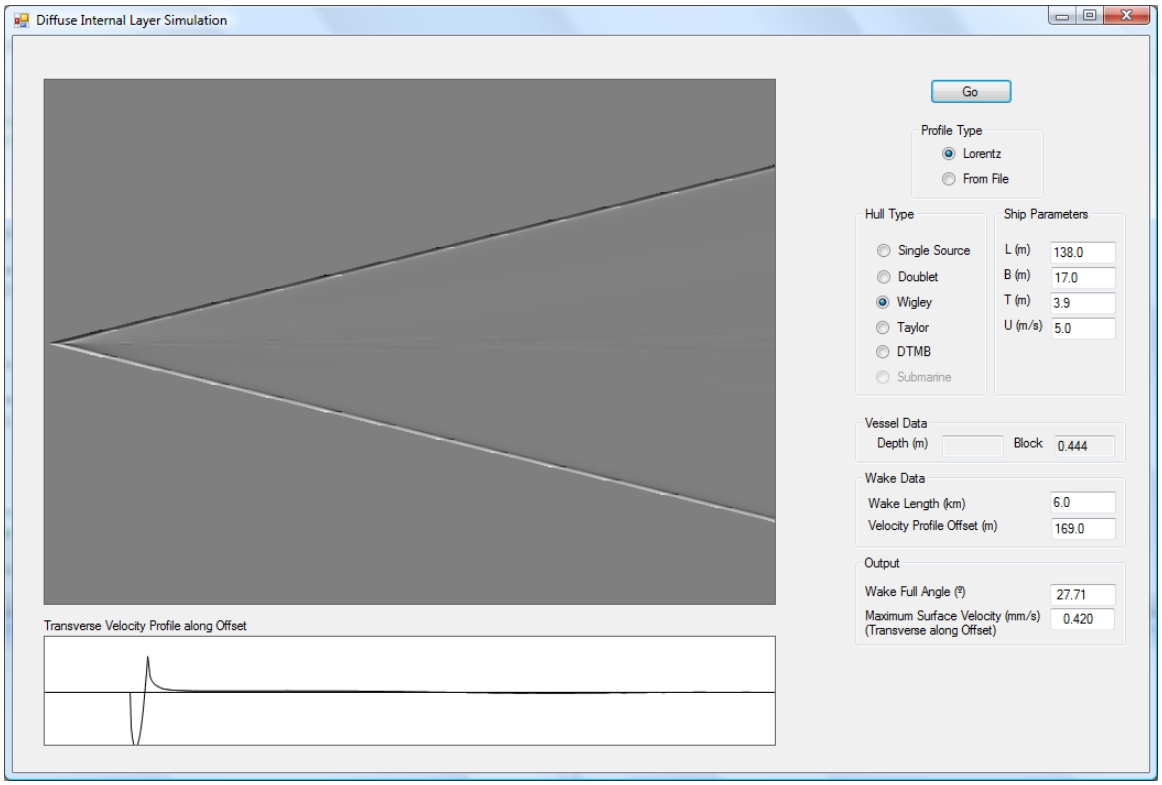

Figure 32. Simulation main window with Gibraltar profile and standard parameters.

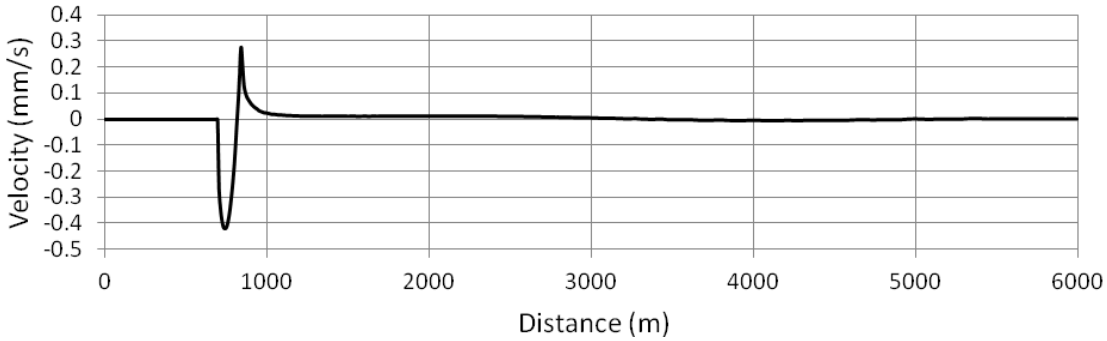

Figure 33. The velocity profile using the Gibraltar layer profile.

Discussion

Given the uncertainties in the flow velocities derived from the observations during the Loch Linnhe trials, mutual comparisons between observations from the trials and the simulations suggest that the models provide reasonable predictions. The diffuse model is clearly superior to the discrete model from both a theoretical point of view, since it more closely represents real layer properties, and from a practical point of view in that it provides a better match to the observations. It is not restricted to narrow layers of the Loch Linnhe type.

Matching of sets of wakes includes their crest patterns and their amplitudes. The crest patterns are an excellent match as has been demonstrated before [6] as well as in the present study. The matching of SAR wake images and velocity patterns is more difficult because it requires a connection between radar scattering coefficients of the ocean surface and the surface flows. This has been bypassed in part by using the derived surface flows from the trials. If we assume that there is an approximately linear relation between the spatial derivatives of the surface flow velocity and the scattering coefficient, as in [9], then there is also a good match between the general appearances of the observed radar wake and the simulated wake.

The wakes from several hull forms have been compared. It has been found that the shape of the hull is not particularly important for internal wave wakes. On theoretical grounds the hull shape should not affect the wake crest pattern but only its amplitudes. However, the effect on the amplitudes is quite minor; this is consistent with findings for the discrete layer.

Changing the ship dimensions affects the amplitudes within the wake; these are approximately proportional to the maximum transverse area of the ship (beam times draft times a mid-ships coefficient). The length of the ship affects how the waves generated by sources and sinks interfere. The wake amplitudes are not a strong function of ship speed As the speed increases the wake narrows and amplitudes tend to grow but quite slowly.

It is important to note that the simulation estimates of the amplitudes very close to the wake edge are sometimes not reliable but this does not affect most of the results here because the amplitudes inside the wake are of the same order. The problem is related to the neglect of internal shock waves and possibly other non-linear phenomena. When the Wigley and other models are used, the source distribution is spread out along the ship's length and this tends to broaden any shock wave at the wake edge and avoids large amplitudes analogous to the sonic boom of a super-sonic aircraft. However, problems can arise when the single source or doublet are employed.

Wake Detectability

Observations from the Loch Linnhe trials suggest that internal wave wakes can be observed in SAR imagery when the surface flow velocities are several centimeters per second and the wavelength of these changes is of the order of 10 m. Using current technology, such as RADARSAT-2 and Sentinel-1, the lower limit for wake detectability is probably of the order of one centimeter per second.

If the wavelength of waves is of the order of 100 m or more, as for the interior of the Gibraltar wake, the internal wave wake generated on a this type of layer is probably difficult to detect by SAR with current technology. This is even in the absence of a mixed layer. The Gibraltar wake mainly comprises a 'V' shape and the width of each wake arm could be small if a ship were moving at high speed. Though this would not necessarily provide a large increase in the wake surface flow velocities, it would increase their derivatives and this could make the wake arms detectable.

The existence of a mixed layer just a few meters deep is sufficient to reduce the surface flows that might be detectable to millimeters per second. The presence of a mixed layer is very common because winds of a few meters per second will create non-linear effects, such as wave breaking that eventually mix the water in the upper ocean to a depth of the order of the wavelength of the surface gravity waves. Therefore it is readily understood why internal wave wakes from surface ships are rare; they will only be detectable when conditions are conducive to the creation of internal layers and the water surface has been calm for a considerable time.

Conclusions

The diffuse model of an internal layer, the wake simulation theory and its implementation in computer code provide results that are consistent with Loch Linnhe trial data and previous simulations using a discrete layer model.

It has been demonstrated that the presence of a surface mixed layer dramatically reduces the wake surface flows when the depth of the layer is greater than the draft of the ship so that the ship does not penetrate the internal layer itself.

The internal wave wake is not sensitive to the hull shape and depends primarily on the principal dimensions of the ship and its velocity.

An internal wave wake that can be identified as such by its internal structure can only be observed when special conditions are met. Thus, a strong layer must exist, it must be close to the surface and the surface mixed layer must be thin. Wakes on weak, deep layers could be observable as a 'V' with no internal structure. Again there must not be a significant mixed layer at the surface. The likelihood of observing a wake on the Gibraltar profile, for example, is enhanced if the ship is traveling at high speed.

The simulations have been based on the simplest of practical models. There are other effects that can enhance wake detectability by increasing the surface flows. One example is the reflection of natural waves from a ship hull. A wave carries momentum and during the reflection process momentum can be transferred from the ship to the wave and greatly increase the wave amplitude. A second example involves a current shear, which can amplify waves, or at least reduce their attenuation. The low ship velocity regime (below the super-critical limit) should be examined.

A significant omission in the simulation is the likelihood of an internal shock wave at the wake edges. This could be important for ships generating wakes on deep layers, such as the Gibraltar layer and should be corrected.

No evidence has been found for soliton wakes but, if they occur, their appearance would resemble the Gibraltar profile wake with two arms and negligible internal structure. There is a possibility that the way in which solitons form by non-linear coalescence of a wave train could also increase the wave amplitudes. This is an interesting theoretical problem.

References

[1] J.K.E. Tunaley, "The theory of internal wave wakes", London Research and Development Corporation final report CR 2012-119 under DRDC Ottawa contract W7714-4500869967, June 2012.

[2] J.K.E. Tunaley, "Simulations of internal wave wakes from the Loch Linnhe trials", London Research and Development Corporation final report CR 2013-048 under DRDC Ottawa contract W7714-4500969321, October 2013.

[3] J.K.E. Tunaley, "Simulation of internal wave wakes and comparison with observations", ESA Living Planet Symposium, Edinburgh, September 2013. Available at www.London-Research-and-Development.com/Publications.html.

[4] K.B. Dysthe and J. Trulsen, "Internal waves from moving point sources", *Johns Hopkins APL Technical Digest*, Vol. 10, No. 4, pp 307-316, 1989.

[5] G. Watson, R. Chapman and J. Apel, "Measurements of internal wave wake of a ship in a highly stratified sea loch", *J. Geophys. Res*., Vol. 97, No. C6, pp 9689-9703, June 1992.

[6] G.G. Hogan, R.D. Chapman, G. Watson and D.R. Thompson, "Observations of ship-generated internal waves in SAR images from Loch Linnhe, Scotland, and comparison with theory and *in situ* internal wave measurements", *IEEE Trans. Geosci. Remote Sens*., Vol. 34, No. 2, pp 532-542, March 1996.

[7] C.R. Jackson, J.C.B. da Silva, G. Jeans, W. Alpers and M.J. Caruso, "Nonlinear internal waves in synthetic aperture radar imagery", *Oceanography*, Vol. 26, No. 2, pp 68-79, http://dx.doi.org/10.5670/oceanog.2013.32, 2013.

[8] C.R. Jackson, J.C.B. da Silva and G. Jeans, "The generation of nonlinear internal waves", *Oceanography*, Vol. 25, No. 2, pp 108-123, http://dx.doi.org/10.5670/oceanog.2012.46, 2012.

[9] W. Alpers "Theory of radar imaging of internal waves", *Nature*, Vol. 314, pp 245-247, http://dx.doi.org/10.1038/314245a0, 1985.

[10] Global Ocean Associates, *An Atlas of Internal Solitary-Like Waves and Their Properties*, 2nd Edition (Prepared under contract to the Office of Naval Research, Code 322PO), 2004. Available at http://www.internalwaveatlas.com.

[11] M. Gertler, "A reanalysis of the original test data for the Taylor Standard Series", Navy Department, David Taylor Model Basin Report 806, March 1954.

[12] F.H. Todd, "Series 60 – Methodical experiments with models of single screw merchant ships", David Taylor Model Basin Report 1712, July, 1963.

[13] D. Hally, “Representation of Wigley hulls by HLLSRF”, Defence Research Establishment Atlantic, Technical Communication 89/308, September, 1989.

[14] J.K.E. Tunaley, “An examination of the Taylor Standard Series of hull forms”, London Research and Development Corporation report at www.London-Research-and-Development.com/Publications.html, 2013.

[15] R. Courant and D. Hilbert, *Methods of Mathematical Physics*, Volume 1, John Wiley & Sons, New York, 1953.

[16] P.M. Morse and H. Feshbach, *Methods of Theoretical Physics, Part 1*, McGraw-Hill Co., Inc., New York, 1953.

[17] J.K.E. Tunaley, “Algorithms for the simulation of the SAR image of a surface ship”, London Research and Development Corporation final report under DRDC Ottawa final report under contract 014ST.W7714-2-9597, September 1992.

[18] I. Chunchuzov, P.W. Vachon and X. Li, “Analysis and modeling of atmospheric gravity waves observed in RADARSAT SAR images”, *Remote Sens. Environment*, Vol. 74, pp 343-361, 2000.

Appendix 1: Sturm-Liouville Theory

In the present context, we are dealing with a simplified Taylor-Goldstein equation, which can be written in the form:

$$\frac{d^2Q}{dz^2} + \lambda\rho(z)Q = 0\,. \tag{8}$$

Here the parameter λ is the square of the horizontal wave number and the function $\rho(z)$ involves the horizontal wave frequency and the B-V frequency. In the standard theory, ρ is always positive but in this application it can be negative. Therefore it is useful to determine if this is an important limitation. The problem is to solve this equation subject to boundary conditions such that Q is zero at $z = 0$ and at $z = L$. This leads to a sequence of eigenvalues, λ_n and eigenvectors Q_n.

The standard approach is to first show that the operator d^2/dz^2 is self-adjoint or Hermitian. This is easily done for the present boundary conditions. In general we need to show that (here the solutions are real so that the complex conjugates are actually not relevant):

$$\int_0^L v^* \frac{d^2u}{dz^2}dz = \left(\int_0^L u^* \frac{d^2v}{dz^2}dz\right)^*. \tag{9}$$

Integrating the left-hand side by parts we have:

$$\int_0^L v^* \frac{d^2u}{dz^2}dz = v^* \frac{du}{dz}\Big]_0^L - \int_0^L \frac{dv^*}{dz}\frac{du}{dz}dz\,. \tag{10}$$

The first term on the right is zero because of the boundary conditions. Another integration by parts shows that the operator is indeed self-adjoint.

Secondly, it is shown that the eigenfunctions are orthogonal. Consider two eigenfunctions, Q_n and Q_m. Multiplying the Taylor-Goldstein equation by Q_m and integrating we have:

$$\int_0^L Q_m \frac{d^2Q_n}{dz^2}dz = -\lambda_n \int_0^L \rho(z)Q_mQ_n dz\,. \tag{11}$$

However, reversing the roles of m and n, we also have:

$$\int_0^L Q_n \frac{d^2Q_m}{dz^2}dz = -\lambda_m \int_0^L \rho(z)Q_nQ_m dz\,. \tag{12}$$

The left-hand sides of (11) and (12) are equal by virtue of the self-adjoint property so that, if the two eigenvalues are different:

$$(\lambda_m - \lambda_n)\int_0^L \rho Q_mQ_n dz = 0\,. \tag{13}$$

Therefore the integral must be zero irrespective of the sign of ρ. This implies that the eigenvectors are orthogonal, if orthogonality is defined in terms of the integral, which includes the weighting function ρ.

When $m = n$, (13) is satisfied automatically. Moreover, except under very special circumstances (namely when $m = n$ and the integral is zero), they can also be normalized and rendered orthonormal, i.e.

$$\int_0^L \rho Q_m Q_n dz = \delta_{mn} . \tag{14}$$

In practice there appear to be no problems in normalizing the eigenfunctions.

Appendix 2: The Crest Pattern and Wake Waves

Figure 34 shows the geometry of wake formation. A disturbance at O, created by ship S propagates at an angle θ to a position in the wake described by angle β.

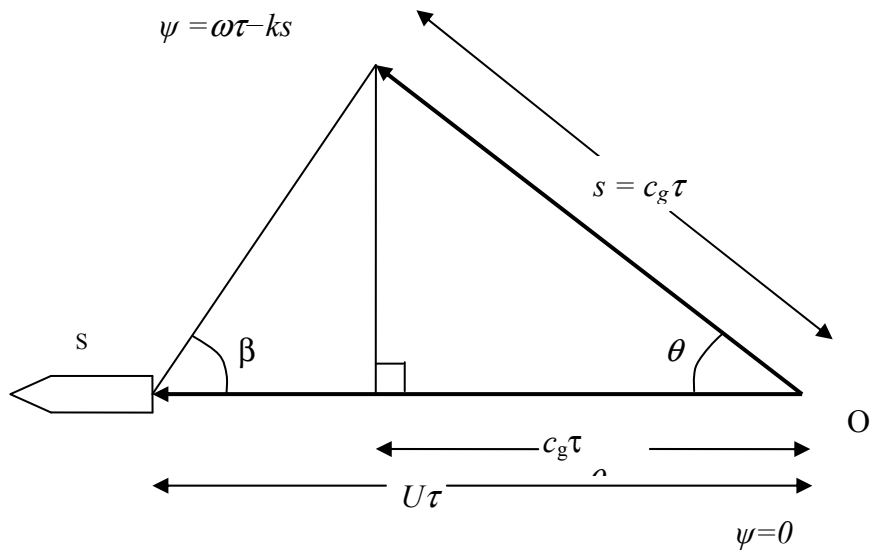

Figure 34. Geometry of wake formation using group velocity concept.

In the far wake the phase is given by:

$$\begin{aligned}\psi &= \omega\tau - ks = (\omega - kc_g)\tau \\ &= k(c - c_g)\tau\end{aligned}, \tag{15}$$

where τ is the propagation time. Therefore, if the crests are separated by 2π and n is an integer indicating the crest number, the time interval is given by:

$$\tau = \frac{2\pi n}{k(c - c_g)} . \tag{16}$$

It follows that, using the phase condition $c = U\cos\theta$, the coordinates in the wake relative to the ship (x, y) are given by:

$$\begin{aligned}x &= (U - c_g \cos\theta)\tau \\ &= \frac{2\pi n U(1 - cc_g / U^2)}{k(c - c_g)} \\ y &= c_g \tau \sin\theta \\ &= \frac{2\pi n c_g \sqrt{1 - c^2 / U^2}}{k(c - c_g)}\end{aligned} . \tag{17}$$

The phase and group velocities are determined from the dispersion relation and each of these can be regarded as a function of either wave frequency or wave number. Therefore the positions along the crests can be plotted out directly from (17).

Because the medium is dispersive, the wake waves, which propagate outwards from a disturbance created by the ship, soon become close to sinusoidal in shape. At each point within the wake they are represented by their amplitude and their wave vector. The wave vector can be found from geometrical considerations. Therefore, in terms of the angle β in Figure 34, we have:

$$\tan\beta = \frac{y}{x} = \frac{\frac{c_g}{U}\sqrt{1-\frac{c^2}{U^2}}}{1-cc_g/U^2}\,. \tag{18}$$

Now c and c_g are functions only of ω or k, so that this can be inverted numerically to give ω or k (which are related by the phase velocity). The direction of **k** can be found from the Doppler equation:

$$c = U\cos\theta \tag{19}$$

Once the wave vector at a point has been determined, the phase, ψ, can be found from the geometry:

$$\psi = -\mathbf{k.r} = -kr\cos(\beta+\theta)\,. \tag{20}$$

However, to evaluate the double integral in Appendix 3, we need to know how the phase varies with θ. We assume that the distance r is large so as to be able to use the stationary phase approach, which is consistent with the concept of group velocity.

Appendix 3: Integral Evaluation

The vertical component of the velocity is given by:

$$q_z(\mathbf{r}') = -\frac{1}{(2\pi)^3}\int \frac{Q_0(z)}{k_0^2 - k^2} S_0 \left(\frac{\partial F_0}{\partial z}\right)_{z=c} e^{-i\mathbf{k}.\mathbf{r}'} d\mathbf{k} \,. \tag{21}$$

The horizontal component, q_r, is found from the divergence, which is zero:

$$\frac{\partial q_z}{\partial z} + \frac{\partial q_r}{\partial r'} = 0 \,. \tag{22}$$

At the surface $q_z = 0$ but the derivative is finite. From (21), we have:

$$q_{r'} = \frac{i}{k}\frac{\partial q_z}{\partial z} \,. \tag{23}$$

The direction of the horizontal flow is given by the angle θ.

We can evaluate q_r:

$$\begin{aligned} q_r &= \frac{iS_0}{(2\pi)^3}\int \frac{1}{k}\frac{\partial}{\partial z}\left(\frac{Q_0(z)}{k_0^2 - k^2}\right)\left(\frac{\partial F_0}{\partial z}\right)_{z=c} e^{-i\mathbf{k}.\mathbf{r}} k dk d\theta \\ &\approx -\frac{S_0}{(2\pi)^2}\int_{-\pi}^{\pi} d\theta \left(\frac{\partial Q_0}{\partial z}\right)_{z=0}\left(\frac{\partial F_0}{\partial z}\right)_{z=c} \frac{e^{-i\mathbf{k_0}.\mathbf{r}}}{2k_0} \\ &\approx -\frac{S_0}{(2\pi)^2 2k_0}\left(\frac{\partial Q_0}{\partial z}\right)_{z=0}\left(\frac{\partial F_0}{\partial z}\right)_{z=c}\sqrt{\frac{2\pi}{|\psi_{\theta\theta}|}} e^{-i(\mathbf{k_0}.\mathbf{r} - \pi/4)} \end{aligned} \,. \tag{24}$$

To find the second derivative of the phase we differentiate (a subscript indicates a derivative):

$$\begin{aligned} \psi_\theta &= k_\theta r\cos(\beta+\theta) - kr\sin(\beta+\theta) \\ \psi_{\theta\theta} &= k_{\theta\theta} r\cos(\beta+\theta)) - 2k_\theta r\sin(\beta+\theta) - kr\cos(\beta+\theta) \end{aligned} \,. \tag{25}$$

Noting that $\psi_\theta = 0$ at a saddle point, the sine term can be eliminated using the first of these equations and we have:

$$\psi_{\theta\theta} = \left(\frac{k_{\theta\theta}}{k} - 2\frac{k_\theta^2}{k^2} - 1\right)\psi \,. \tag{26}$$

The derivatives of k can be found from the equation $c = U\cos\theta$. Then we have:

$$\begin{aligned} \frac{dc}{dk}k_\theta &= -U\sin\theta \\ \frac{d^2c}{dk^2}k_\theta^2 + \frac{dc}{dk}k_{\theta\theta} &= -U\cos\theta \end{aligned} \,. \tag{27}$$

Therefore, noting that

$$\begin{aligned} \frac{dc}{dk} &= -\frac{c - c_g}{k} \\ \frac{d^2c}{dk^2} &= \frac{1}{k}\frac{dc_g}{dk} + 2\frac{c - c_g}{k^2} \end{aligned} \,. \tag{28}$$

we have:

$$k_\theta = \frac{kU\sin\theta}{c - c_g}$$

$$k_{\theta\theta} = \frac{kU\cos\theta}{c - c_g} + \frac{k^3U^2\sin^2\theta}{(c - c_g)^3}\frac{d^2c}{dk^2} \quad . \tag{29}$$

$$= \frac{kU\cos\theta}{c - c_g} + \frac{k^3U^2\sin^2\theta}{(c - c_g)^3}\left(\frac{1}{k}\frac{dc_g}{dk} + 2\frac{c - c_g}{k^2}\right)$$

Combining these results yields:

$$\psi_{\theta\theta} = \left(\frac{U\cos\theta}{c - c_g} + \frac{kU^2\sin^2\theta}{(c - c_g)^3}\frac{dc_g}{dk} - 1\right)\psi \, . \tag{30}$$

Appendix 4: Matrix Approach

The Runge-Kutta and similar methods of integration can introduce small errors. These can be very important when finding the eigenvalues and eigenvectors. The problem occurs when the frequency approaches the maximum B-V frequency when the eigenvectors fall to extremely small values at both ends of their range; this leads to rapid variations that imply that the integration step size should be reduced. The results tend to contain errors that make it impossible for the search for an eigenvalue and particularly the eigenvector to succeed. The eigenvalue may be reasonable but the apparent eigenvector may contain a large positive or negative spike at the end corresponding to the ocean floor.

The R-K algorithm is not wholly responsible for this problem but uncertainties over its accuracy can be avoided by turning to a matrix approach in which the layer is exactly treated in a step-wise manner. Within each step, the Taylor-Goldstein equation can be solved explicitly and the boundary conditions matched. The solution at the *n*th step takes one of the following forms, depending on the sign of the final term in the Taylor-Goldstein equation, specifically the ratio of the BV frequency at a given depth to the frequency:

$$y = \begin{cases} Ae^{k_n z} + Be^{-k_n z}, & k_n^2 < 0 \\ A\cos(k_n z) + B\sin(k_n z), & k_n^2 \geq 0 \end{cases}. \tag{31}$$

Here A and B are constants, z is the distance from the start of a step and, from the Taylor-Goldstein equation, k_n is given by:

$$k_n^2 = k^2\left(\frac{N_n^2}{\omega^2} - 1\right). \tag{32}$$

In terms of the amplitude, y, and its derivative with respect to depth, y', in the first case we have:

$$\begin{aligned} y_n &= A + B \\ y_n' &= k_n(A - B) \end{aligned}. \tag{33}$$

Solving we have:

$$\begin{aligned} A &= \frac{1}{2}\left(y_n + \frac{y_n'}{k_n}\right) \\ B &= \frac{1}{2}\left(y_n - \frac{y_n'}{k_n}\right) \end{aligned}. \tag{10}$$

Therefore, if the distance between steps is d, the amplitude and its derivative at step n+1 are:

$$\begin{aligned} y_{n+1} &= \frac{1}{2}\left(y_n + \frac{y_n'}{k_n}\right)e^{k_n d} + \frac{1}{2}\left(y_n - \frac{y_n'}{k_n}\right)e^{-k_n d} \\ y_{n+1}' &= \frac{k_n}{2}\left(y_n + \frac{y_n'}{k_n}\right)e^{k_n d} - \frac{k_n}{2}\left(y_n - \frac{y_n'}{k_n}\right)e^{-k_n d} \end{aligned}. \tag{34}$$

These equations can be put into matrix form:

$$\begin{pmatrix} y_{n+1} \\ y'_{n+1} \end{pmatrix} = \begin{pmatrix} \cosh(k_n d) & \sinh(k_n d)/k_n \\ k_n \sinh(k_n d) & \cosh(k_n d) \end{pmatrix} \begin{pmatrix} y_n \\ y'_n \end{pmatrix}. \tag{35}$$

The result for the oscillatory solution is identical when we take k_n^2 to be negative, or in other words:

$$\begin{pmatrix} y_{n+1} \\ y'_{n+1} \end{pmatrix} = \begin{pmatrix} \cos(k_n d) & \sin(k_n d)/k_n \\ -k_n \sin(k_n d) & \cos(k_n d) \end{pmatrix} \begin{pmatrix} y_n \\ y'_n \end{pmatrix}, \tag{36}$$

where k_n is now real.

To determine the eigenvalues, k, and the corresponding eigenvectors a search can be implemented to find the eigenvalue that matches the boundary conditions both at the surface and at the bottom. The eigenvector is then the sequence of amplitudes at each step.

Appendix 5: Comparison of Discrete and Diffuse Layer Theories

It was considered to be useful to compare the theories for the discrete and diffuse layers to ensure that they were consistent with each other; therefore they were less likely to be invalid. The discrete layer theory was based on the velocity potential, which provides the surface velocity components quite directly, whereas the diffuse theory relies on the zero divergence of the velocity at the surface.

In the case of a discrete layer we work in terms of the velocity potential. Near the surface, for both the discrete and diffuse cases we expect this to be given approximately by:

$$\Phi = F\cosh(kz)e^{-i\mathbf{k.r}} \quad , \tag{37}$$

where F is a function of the other parameters including the dispersion relation. It follows that the vertical and the surface velocities are given by:

$$\begin{aligned} v_z &= \frac{d\Phi}{dz} = kF\sinh(kz)e^{-i\mathbf{k.r}} \\ v_r &= \frac{d\Phi}{dr} = ikF\cosh(kz)e^{-i\mathbf{k.r}} \end{aligned} \quad . \tag{38}$$

It follows that the vertical fluid velocity is zero at the surface ($z = 0$) but the horizontal components are finite.

For the diffuse layer, the solution near the surface is proportional to dv_z/dz. For either layer, this is given by:

$$\frac{dv_z}{dz} = k^2 F\cosh(kz)e^{-i\mathbf{k.r}} \; . \tag{39}$$

This is finite at the surface. Now comparing the calculation with that using the divergence of the velocity (as for the diffuse layer) yields:

$$v_r = \frac{i}{k}\frac{dv_z}{dz} = ikF\cosh(kz)e^{-i\mathbf{k.r}} \; . \tag{40}$$

This is the same as in (38). Therefore the two approaches are consistent. The factor of k in (40) ensures that the amplitude of the horizontal velocity near the wake edge does not go to infinity.